Numerical simulation of continuum scale electrochemical hydrogen bubble evolution

Kurian J. Vachaparambil, Kristian Etienne Einarsrud*

Department of Materials Science and Engineering, Norwegian University of Science and Technology (NTNU), Trondheim 7491, Norway

ABSTRACT

One of the important aspects in improving the efficiency of electrochemical processes, such as water electrolysis, is the efficient removal of bubbles which evolve from the electrodes. Numerical modelling based on Computational Fluid Dynamics (CFD) can describe the process, provide insights into its complexity, elucidate the underlying mechanisms of how bubbles evolve and their effect as well as aid in developing strategies to reduce the impact of the bubble.

In this paper, a Volume of Fluid (VOF) based simulation framework to study the evolution of hydrogen bubbles in the order of few hundred micrometers, refered to as continuum scale bubbles, is proposed. The framework accounts for the multiphase nature of the process, electrochemical reactions, dissolved gas transport, charge transport, interfacial mass transfer and associated bubble growth. The proposed solver is verified, for two-dimensional cases, by comparison to analytical solution of bubble growth in supersaturated solutions, stationary bubble, rising bubbles and qualitative analysis based on experimental observations of the variations in current based on static simulations. The proposed solver is used to simulate the evolution of a single bubble under various wetting conditions of the electrode as well as the coalescence driven evolution of two bubbles. The results show that as the bubbles detach, its surface oscilates and the shape of the rising bubble is determined by the balance between drag force and surface tension. These surface oscillations, which causes the bubble to get flattened and elongated, results in temporal variation of the electrical current. The reduction of current due to bubble growth is visible only when these surface oscillations have reduced. The simulations also show the current as a function of the position of the bubble in the interelectrode gap. The framework also predicts the increase in current as a result of bubbles leaving the surface which is larger when the process is coalescence driven. The simulations indicate that bubble coalescence is the underlying mechanism for continuum scale bubble detachment.

* Corresponding author.:.
E-mail address: kristian.e.einarsrud@ntnu.no (K.E. Einarsrud).

1. Introduction

One of the potential ways to address the intermittencies in energy production via renewable sources is to convert surplus energy into hydrogen using water electrolysis. This hydrogen can be used as an energy vector which would reduce the dependence on fossil fuels, reduce carbon footprint and foster the move to the environmentally-benign hydrogen economy [1]. In order to enable this transition, the cost of hydrogen production from water electrolysis must be reduced using cheaper electricity from renewable sources on energy (as electricity can account upto 70% of the costs [1]) and more efficient water electrolyzers. On going research into making efficient water electrolyzers has been focused primarily on the development of active and durable electrocatalysts for the water splitting reactions, see [2–4]. Another aspect to improve the efficiency of the electrolyzer is to remove bubbles, which reduce the area of the electrode in contact with electrolyte as well as the effective electrolyte conductivity, see [5,6]. Additionally, convection associated with bubble evolution has been reported to increase mass transfer rates in the electrochemical systems [6]. As efficient removal of bubbles during water electrolysis can result in saving 10–25% of the energy supplied [5], understanding the dynamics of bubble evolution can aid in developing strategies to improve the efficiency of the water electrolyzers.

Although experimental works have provided substantial insights into the physics underlying the electrochemical gas evolution, [7–10], numerical simulations can provide a fundamental understanding of the coupled nature of the process as well as the temporal and spatial variations of the flow parameters as bubbles evolve. As electrochemical gas evolution is a multiphysics-multiscale process, the choice of numerical simulations employed depends on the phenomena of interest, see [11]. Broadly speaking, atomistic process like the electrochemical reactions and the bubble nucleation [12] are typically studied using molecular dynamic simulations [13] whereas continuum scale process (which are few hundred micrometer or larger) like bubble growth and detachment can be studied using Computational Fluid Dynamics (CFD) [14] and the intermediate scales relevant for ion migration and continuous bubble evolution can be investigated using meso-scale models like Lattice Boltzmann method [15,16]. This paper delves into the evolution of continuum scale hydrogen bubbles, which are few hundred micrometers in radius, observed in experimental works like [7–9], which are studied using multiphase-multiphysics CFD approaches.

In order to study the dynamics of continuum scale electrochemical bubble evolution it is necessary to simulate the relevant multiphysics, summarized in Fig. 1. The numerical modelling of *multiphase flows* can be divided into dispersed phase and interface resolved modelling [17]. Dispersed phase modelling (which includes Euler-Euler, Mixture and Euler-Lagrange approaches) requires closure models to describe the momentum transfer between the phases as the individual bubbles are not resolved. These momentum closure terms relies on the assumption of a bubble size which is typically set based on experimentally observed detachment diameter, see [18]. The dispersed phase modelling approaches, which are used in majority of the numerical simulation of the electrochemical gas evolution, see the review by [18,19] or works like [19,20], are typically employed to study the dynamics of industrial scale electrolyzers where the larger flow features are of interest. On the other hand interface resolved modelling approaches, like the Volume of Fluid (VOF), are typically used to study the detailed behaviour of the interface without having to use approximations in order to capture the momentum transfer between the phases like in dispersed phase modelling. As a result of resolving the bubble, VOF provides an ideal framework to study the details of evolution of bubbles which are of interest in this work. The VOF model uses a scalar, the
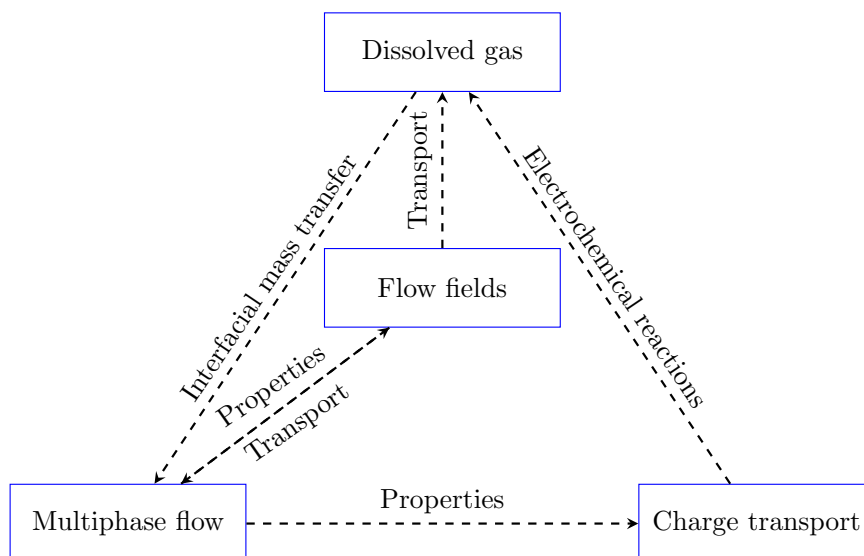

Fig. 1. Illustration of the coupled nature of electrochemical gas evolution.

volume fraction of liquid (α_1), to identify the bubble, liquid and interface which corresponds to α_1 equal to zero, unity and (0,1) respectively [17]. The interface is captured by advecting α_1 and the sharpness of the interface is ensured by using either the computationally cheaper algebraic VOF, see [21], or the sharper but computationally more demanding geometric VOF, see [22]. Both these methods generate numerical artifacts known as 'spurious velocities' due to inaccuracies in calculating the interfacial curvature and inconsistent descritization, see discussion in [21]. It should be noted that the sub-cell level reconstruction of interface in the geometric VOF method generates smaller spurious velocities when compared to algebraic VOF methods, but this geometric reconstruction of interface is more computationally demanding and has some limitations in its application, see [21–23]. These spurious velocities, which are dominant when simulating surface tension driven flows, are very well studied in literature [21,22,24–26]. Readers interested in the source of these spurious velocities and review of on-going research to address them are referred to works like [24]. Due to the computational cost associated with using geometric VOF and challenges related to its implementation, algebraic VOF methods are very commonly used to study two phase flow scenarios including surface tension dominant flows [21,25–31].

Another relevant feature in electrochemical gas evolution of continuum scale bubble is the transport of the *dissolved gas* which requires treatment of interfacial jump conditions for concentration across the interface and interfacial transmission condition (which ensures that the interface does not accumulate the species), see [28,32]. Two ways to simulate the species transport are single and two field approaches. The two field approach, described by [32,33], uses individual transport equations for species in each phase and the interfacial jump conditions are treated like boundary conditions for each phase. The single field approach, described by [28,29], uses a unified governing equation that accounts for the interfacial jump conditions to describe the transport of species in both phases. Although dissolved gas, which is present only in the liquid phase, transport can be simulated by both these approaches by limiting mass transfer across the interface (like described in [27]), two and single field approaches are recommended to be used with geometric and algebraic VOF methods respectively, see [28]. Once the dissolved gas distribution is known, the *interfacial mass transfer* and the associated *bubble growth* can be computed based on Fick's 1st law (see [27,34,35]) or with flow scenario based Sherwood number based correlations (see [36]). As Sherwood number correlations are applicable for specific flow scenarios [34], bubble evolution, which is associated with complex flow patterns as well as interface deformation, cannot be accurately described by a single Sherwood number correlation to the best of the authors' knowledge.

Another aspect of simulating electrochemical gas evolution is the *charge transport*, which drives the electrochemical reactions as it is proportional to the current density, based on Faraday's law of electrolysis. Due to the insulating nature of bubbles, their presence results in a redistribution of current, which increases the electrical resistance [37,38]. The commonly used approach to ensure charge conservation is based on Gauss's law, one of the four Maxwell's equations for electromagnetism, and current density expressed based on the Ohm's law which has been used in works like [39,40]. A benefit of using the interface resolved approach, like VOF, is that the effective conductivity of the heterogenous media, i.e. bubble-electrolyte, can be computed without having to use semi-empirical relations, like the Bruggeman correlation [6], which is required in dispersed phase modelling approaches [19,20] as shown by [41].

Due to the coupled multiphysics relevant in electrochemical gas evolution, literature which employs interface resolved simulations to study the dynamics of electrochemically generated bubbles are quite limited to the best of the knowledge of the authors. These works can be divided into pure and hybrid VOF methods. In 'pure' VOF methods, like [36], the evolution of a single hydrogen bubble was studied by simulating the growth driven by interfacial mass transfer (based on Sherwood number) without accounting for the charge transport. In our previous work [41], we described the various modules needed to simulate continuum scale electrochemical gas evolution, see Fig. 1, in a decoupled manner in addition to briefly illustrating the potential of fully coupled VOF solver via simulation of a single sliding bubble on a vertical electrode. Although not based on VOF approach, the recent work by [42] used another interface resolved approach, based on the Front Tracking method, to study the impact of bubble evolution induced convection on ionic transport in water electrolysis. In 'hybrid' VOF approaches, like [39,40,43], VOF was coupled with sub-grib bubbles treated via dispersed modelling approaches and the resolved bubble were assumed to grow only via coalescence. These hybrid VOF, typically used to simulate the carbon dioxide evolution at the anode during aluminium production, is used to simulate bubble evolution on an whole electrode[39,40]. reported the transient evolution of voltage (under constant current condition) as result of bubble evolution from the electrode whereas [43] did not simulate the current distribution nor the transport of dissolved gas generated from the electrochemical reactions. Apart from these studies, other simplified studies have employed interface resolved simulations to investigate the behaviour of the interface without considering any multiphysics effects like [44]. Although the previous works have provided substantial knowledge into the modelling of evolution of electrochemically generated bubbles, there is still a lack of computational models that treat the complexity associated with the multiphysics and multiscale nature of the process as highlighted in the recent review by [11]. Additionally, bubble evolution during water electrolysis due to coalescence, observed in experimental studies like [7,8,10], has not been investigated extensively using numerical simulations as discussed in the review by [45].

In this paper, which is based on our recent work which was presented at CFD2020 [41], we address this lack of knowledge by developing a coupled multiphysics solver that can handle the continuum scale hydrogen bubble evolution during water electrolysis. The proposed solver is based on the algebraic VOF framework available in OpenFOAM® 6 which is modified to account for transport of dissolved gas [29] along with the associated supersaturation driven bubble growth (based on [27]) and charge transport (based on Gauss's law and Ohm's law, see [39]) which are coupled based on electrochemical

reaction defined based on Faraday's law of electrolysis. In order to reduce the complexity, the proposed solver is developed based on the following simplifications/assumptions:

- The bubble evolution and the electrochemical reactions occurs only at the cathode and the anode/counter-electrode is assumed to not affect the process,
- The proposed model treats the evolution of only continuum scale bubbles, which are in the order of few hundred micrometers,
- The liquid and the continuum scale bubbles treated in the simulations are assumed to have a constant density and viscosity,
- The flow is assumed to be isothermal and laminar,
- The interface is assumed to be always saturated and saturation concentration is assumed to be constant with the variation of hydrostatic pressure and Laplace pressure in sub-millimeter sized bubbles as it evolves,
- The proposed solver assumes a constant value of surface tension in the simulations. This assumption results in not treating gradients in surface tension which has been observed to generate Marangoni convection during electrochemical hydrogen evolution [9,46],
- The interfacial mass transfer is treated using the Fick's 1st law as the mass transfer coefficients are unknown a priori,
- The spatial and temporal gradient of ions in the computational domain is assumed to be negligible due to the high concentration ions present typically in the electrolyte used for water electrolysis [47],
- The system is assumed to be under constant potential difference, so the bubble evolution leads to changes in current. The proposed solver accounts for the current variation as a result of the ohmic contribution of the bubbles present in the bulk and on the surface. The change in current due to the contributions from the surface and concentration overpotentials, see [48], as a result of bubble evolution is neglected in this paper.

The ability of the proposed solver is showcased via 2D simulations of the evolution of the single hydrogen bubble from cathode for various wetting condition at the electrode. In addition to single bubble simulations, the evolution of bubble driven by coalescence is also investigated. The temporal change in the current as bubble evolves is analyzed for these cases. The novelty of the proposed solver, when compared to previous works that employ multiphysics based interface resolved simulations like [36,42,44], is its ability to simulate coupled phenomena related to dissolved hydrogen transport, interfacial mass transfer due to supersaturation and current variation as a result of bubble evolution driven by coalescence and bubble growth. In the interest of knowledge dissemination and to encourage further scientific advances, the proposed solver will be released at GitHub [49].

2. Proposed solver

2.1. Governing equations

In the Volume of Fluid (VOF) method, see [21,50], the interface and the two phases are represented using a volume averaged scalar called volume fraction of liquid (α_1), defined as

$$\alpha_1(\vec{x}, t) = \begin{cases} 0 \text{ (within Phase 2 or gas)} \\ 0 < \alpha_1 < 1 \text{ (at the interface)} \\ 1 \text{ (within Phase 1 or liquid).} \end{cases} \tag{1}$$

Based on value of α_1, the volume fraction of gas (α_2) is calculated as $1 - \alpha_1$. A single field description of the governing equations for the simulation of multiphase flows can be developed by conditional volume-averaging technique which involves conditioning the conservation equation valid in liquid and gas regions for phase discrimination and its subsequent volume averaging, see [28,51] for details. This conditional volume-averaging technique is used to obtain the single field equations for continuity, momentum and volume fraction transport used by VOF approach, this derivation is discussed in [28,52,53]. For the sake of simplicity, only the final forms of these equations used in the VOF approach, after the notations of conditional volume-averaging are dropped, are described in this work which is similar to representation used commonly in literature [21,25–27,29,50,51].

The interface dynamics are captured using a transport equation of liquid volume fraction:

$$\frac{\partial \alpha_1}{\partial t} + \nabla \cdot (\vec{U}_1 \alpha_1) = \dot{S}_\alpha, \tag{2}$$

where $\vec{U}_1$ is the velocity of the liquid phase and $\dot{S}_\alpha$ is a source term that accounts for bubble growth [50]. A single field description of the velocity ($\vec{U}$) can be described as

$$\vec{U} = \alpha_1 \vec{U}_1 + \alpha_2 \vec{U}_2, \tag{3}$$

where $\vec{U}_1$ and $\vec{U}_2$ are the velocity fields in liquid and gas phase respectively [50]. The relative velocity between the two phases ($\vec{U}_r$) is computed as

$$\vec{U}_r = \vec{U}_1 - \vec{U}_2. \tag{4}$$

Now $\vec{U}_1$ is defined in terms of the single field formulation of velocity ($\vec{U}$) and relative velocity ($\vec{U}_r$) as $\alpha_1 \vec{U}_1 = \alpha_1 \vec{U} + \alpha_1(1 - \alpha_1)\vec{U}_r$, from $\alpha_1 \times$ Eq. 3 and $\alpha_1(1 - \alpha_1) \times$ Eq. 4 (see [50]), which can be used to rewrite Eq. 2 as

$$\frac{\partial \alpha_1}{\partial t} + \nabla \cdot (\alpha_1 \vec{U}) + \nabla \cdot (\alpha_1(1 - \alpha_1)\vec{U}_r) = \dot{S}_\alpha. \tag{5}$$

The third term in Eq. 5, which is non-zero only at the interface due to the product $\alpha_1(1 - \alpha_1)$, is used to sharpen the interface. Eq. 5 belongs to Algebraic VOF method, see [21], and the calculation of $\vec{U}_r$ is estimated based on Eq. 21 [25–27,54]. The source term used in Eq. 5 to treat the bubble growth is computed based on works like [27,34] as

$$\dot{S}_\alpha = \alpha_1 \nabla \cdot \vec{U}. \tag{6}$$

The fluid properties (χ) like density (ρ), viscosity (ν) and electrical conductivity (Γ) are calculated based on volume fraction weighted average as

$$\chi = \alpha_1 \chi_1 + \alpha_2 \chi_2. \tag{7}$$

The continuity equation is written as

$$\nabla \cdot \vec{U} = \frac{\dot{m}}{\rho}, \tag{8}$$

where term on the right side on the above equation accounts for the bubble growth due to supersaturation and $\dot{m}$ is computed based on Eq. 17.

The momentum equation is

$$\frac{\partial \rho \vec{U}}{\partial t} + \nabla \cdot (\rho \vec{U}\vec{U}) = -\nabla p + \nabla \cdot \left(\mu(\nabla \vec{U} + \nabla \vec{U}^T) \right) + \rho \vec{g} + \vec{F}_{ST}, \tag{9}$$

where $\vec{F}_{ST}$ accounts for surface tension, $\vec{g}$ is the acceleration due to gravity and $\nabla \cdot \left(\mu(\nabla \vec{U} + \nabla \vec{U}^T) \right)$ is the viscous term. Defining p_{rgh} as equal to $p - \rho \vec{g} \cdot \vec{x}$, $-\nabla p + \rho \vec{g}$ can be written as $-\nabla p_{rgh} - \vec{g} \cdot \vec{x} \nabla \rho$ [21]. The viscous terms in the momentum equation, $\nabla \cdot \left(\mu(\nabla \vec{U} + \nabla \vec{U}^T) \right)$ can be written as $\nabla \cdot (\mu \nabla \vec{U}) + \nabla \vec{U} \cdot \nabla \mu$, see [21,28]. The surface tension term is computed using the Sharp Surface Force (SSF) model, described in [25,26], as

$$\vec{F}_{ST} = \sigma \kappa_{final} \nabla \alpha_{sh}, \tag{10}$$

where κ_{final} is the interface curvature (whose calculation is described in Appendix A) and α_{sh} is the sharpened volume fraction of phase 1 which is determined as

$$\alpha_{sh} = \frac{1}{1 - C_{sh}} \left[\min\left(\max\left(\alpha_1, \frac{C_{sh}}{2} \right), 1 - \frac{C_{sh}}{2} \right) - \frac{C_{sh}}{2} \right], \tag{11}$$

where C_{sh} is a user defined sharpening coefficient $C_{sh} \in [0, 1)$, see [26] for discussion on its influence. Additional notes on the surface tension modelling is available in Appendix A.

Now substituting the definitions of p_{rgh}, viscous terms and surface tension term using SSF model in Eq. 9 to get

$$\frac{\partial \rho \vec{U}}{\partial t} + \nabla \cdot (\rho \vec{U}\vec{U}) = -\nabla p_{rgh} + \nabla \cdot (\mu \nabla \vec{U}) + \nabla \vec{U} \cdot \nabla \mu - \vec{g} \cdot \vec{x} \nabla \rho + \sigma \kappa_{final} \nabla \alpha_{sh}. \tag{12}$$

The transport of species needs to account for concentration jump across the interface in addition to interfacial transmission condition apart from species transport in each phase, see [28]. A single field formulation of the species transport can be obtained by conditional volume-averaging of species transport equation in each phase along with incorporating the aforementioned interface jump conditions, see [28] for derivation. A variant of the single field formulation for species transport is the Compressive Continuous Species Transfer (CCST) model, which was proposed by [29], :

$$\frac{\partial C_i}{\partial t} + \nabla \cdot (\vec{U}C_i) = \nabla \cdot \left(\hat{D}_i \nabla C_i - \hat{D}_i \mathcal{B} C_i \nabla \alpha_1 - \mathcal{B} \alpha_1 \alpha_2 \vec{U}_r C_i \right) + S_i, \tag{13}$$

where S_i is a sink term (computed in Eq. 18), $\mathcal{B}$ is equal to $(1 - He_i)/(\alpha_1 + \alpha_2 He_i)$, He_i describes concentration jump condition (ratio of the species concentration in gas phase to liquid phase at the interface), $\vec{U}_r$ is the compressive velocity defined in Eq. 21, and $\hat{D}_i$ is the harmonic average of the diffusion coefficients of the phases. It should be pointed out that the conditional volume-averaged notations of the derived single field formulation of species transport equation is dropped in Eq. 13 for simplicity, similar to [29]. Using the single field formulation of concentration in CCST, dissolved hydrogen can be simulated by limiting the interfacial mass transfer, that is inherently treated using the interfacial jump conditions, by setting He_i to a small value [27,34,41]. An additional consequence of using a small value of He_i is that the C_i at the interface becomes close to zero which can be interpreted as the concentration field obtained from CCST which is over the saturation condition, see [27,34].

As a result of simulating the dissolved gas, the treatment of interfacial mass transfer and associated bubble growth require determination of the source term in Eq. 8 and sink term at interface for dissolved gas in Eq. 13. In this paper, these

source and sink terms are calculated based on the approach initially developed for evaporation [55,56] and subsequently extended for supersaturation driven bubble growth [27,34]. The driving force for interfacial mass transfer is computed based on Fick's 1st law as

$$j = M_i D_{i,1} |\nabla C_i|, \tag{14}$$

where M_i is the molar mass of hydrogen (i) and $D_{i,1}$ is the diffusion coefficient of the hydrogen in the liquid [27,34]. It should be noted that Eq. 14 is based on the assumption that the concentration gradient in the tangential direction to interface is negligible and this approximation is consistent with the derivation of the single field formulation of species transport, i.e. Eq. 13, see [28]. The above formulation of driving force for interfacial mass transfer implicitly assumes that the species are dilute, while this is strictly not the case in a general setting, we use this formulation as a basis of our framework. Based on Eq. 14, the local mass transfer rate is computed at the liquid side of the interface as

$$\psi_0 = N j \alpha_1 |\nabla \alpha_1|, \tag{15}$$

where N is normalization factor computed as $\int_\Omega |\nabla \alpha_1| dV / \int_\Omega \alpha_1 |\nabla \alpha_1| dV$, see [27,55,56]. ψ_0 is smeared, as proposed by [27,55,56], using:

$$D\Delta t \nabla^2 \psi = \psi - \psi_0, \tag{16}$$

where $D\Delta t$ is the user defined value which controls the extent of smearing. Using ψ, the source term for the continuity equation which accounts for the bubble growth, is redistributed in the region where $\alpha_1 < 0.001$ as

$$\dot{m} = A \alpha_2 \psi, \tag{17}$$

where A is a normalization factor computed as $\int_\Omega \psi_0 dV / \int_\Omega \alpha_2 \psi dV$, see [27,55,56]. This procedure to define $\dot{m}$, which is described further in the work by [55,56], enables the interface to get advected just by the velocity field, without being influenced by the source term. The sink term for the dissolved hydrogen to account for the interfacial mass transport is computed at the liquid side of the interface as

$$S_i = -\frac{N \alpha_1 (j |\nabla \alpha_1|)}{M_i}, \tag{18}$$

where N is the normalization factor used in Eq. 15, see [27,34]. Generation of dissolved hydrogen causing supersaturation in the vicinity of the electrode due to electrochemical reactions, which are proportional to the local value of current density, are added as boundary conditions (further described in Section. 3.1). The charge conservation is solved based on Gauss's law as

$$\nabla \cdot \vec{i} = 0, \tag{19}$$

where $\vec{i}$ is the local current density which is calculated based on Ohm's law as

$$\vec{i} = -\Gamma \nabla \Phi \tag{20}$$

where Γ is the volume fraction weighted average electrical conductivity, based on Eq. 7, and Φ is the electrical potential. It should be noted that Eq. 20 is obtained from Nernst-Planck equation under the assumption of negligible spatial and temporal gradients of ions in the computational domain i.e. electroneutrality, see [57]. This approximation can be physically motivated by high concentrations of ions present in the electrolyte which is typically used for water electrolysis, see [47]. Eq. 19 and Eq. 20 has been previously used to simulate charge transport in electrochemical gas evolution in works like [39–41].

2.2. Solution algorithm and numerical details

The proposed solver is developed based on the VOF solver in OpenFOAM® 6, interFoam, which supports algebraic VOF based simulation of two imcompressible and isothermal flow without any phase change. The proposed solver adds modules, illustrated in Fig. 1, to interFoam in order to enable treatment of the multiphysics coupling relevant in continuum scale electrochemical hydrogen evolution. The overall solution algorithm can be summarized as:

1. Compute α_1 by solving Eq. 5 using the semi-implicit Multidimensional Universal Limiter with Explicit Solution (MULES) method which uses a implicit predictor and explicit corrector steps to ensure the boundedness of α_1 between zero and unity [21,58]. Once α_1 is computed, the volume fraction of phase 2 or bubble (α_2) is computed as $\alpha_2 = 1 - \alpha_1$. In a single field formulation of velocity, $\vec{U}_r$ which is used in the surface compression term in the volume fraction advection equation, Eq. 5, is unknown and estimated, based on [25–27,54], as

$$\vec{U}_r = C_\alpha \left| \frac{\phi}{|\vec{S}_f|} \right| \vec{n}, \tag{21}$$

where $\vec{n}$ is the unit normal to the interface, $\vec{S}_f$ is the area vector of the cell face, ϕ is the volume flux, and C_α is the user defined compression factor which is usually set between values of zero and four [59,21,25].

Table 1
Discretisation schemes.

Modelling term	Keyword	Scheme
Time derivatives	ddtSchemes	Euler [61]
Divergence term	$\nabla \cdot (\rho \vec{U} \vec{U})$ $\nabla \cdot (\vec{U} \alpha_1)$, $\nabla \cdot (\vec{U} C_i)$ $\nabla \cdot (\vec{U_r} \alpha_1 (1 - \alpha_1))$ $\nabla \cdot (\hat{D}_i \mathcal{B} C_i \nabla \alpha_1)$ $\nabla \cdot (\mathcal{B} \alpha_1 \alpha_2 \vec{U_r} C_i)$	vanLeerV [61] vanLeer [61] interfaceCompression [21,61] vanLeer [29,61] vanLeer [29,61]
Gradient term	gradSchemes	linear [61]
Laplacian term	laplacianSchemes	linear corrected [61]
Other	snGradSchemes interpolationSchemes	corrected [61] linear [61]

Table 2
Solvers used for the discretised governing equations, see [61] for further details.

Flow variable	Linear solver	Smoother/ preconditioner	Tolerance
p_{rgh}	PCG	GAMG	10^{-10}
$\vec{U}$	smoothSolver	symGaussSeidel	10^{-10}
α_1	smoothSolver	symGaussSeidel	10^{-10}
Φ	GAMG	DICGaussSeidel	10^{-10}
C_i	PBiCGStab	diagonal	10^{-10}
ψ	GAMG	DICGaussSeidel	10^{-10}

2. Once the interface is known at the current time step, fluid properties (i.e. density and viscosity) is computed based on Eq. 7.
3. The driving force for interfacial mass transfer is then computed based on the Fick's 1st law, i.e. Eq. 14, which is then used to compute the local mass transfer rate (ψ_0) using Eq. 15.
4. In order to improve numerical stability, ψ_0 is smeared to obtain ψ based on Eq. 16.
5. Now solve continuity and momentum equations, i.e. Eq. 8 and Eq. 12, are solved using Pressure Implicit with Splitting of Operators (PISO) algorithm [60]. This can be briefly summarized as iterative procedure in which predicted velocity field is corrected based on pressure correction equation, see [21] for details of the implemented algorithm.
6. Compute the electrical potential and current density using Eq. 19 and Eq. 20.
7. Solve for the dissolved hydrogen transport based on Eq. 13.
8. Advance to the next time step. Adaptive time stepping is used in the simulations to allow for computing the time step such that maximum Courant number, which is defined by the user, is always satisfied. If a maximum time step is defined, the solver takes the minimum of the user defined maximum time step and the time step associated with the Courant number [61].

All the variables are stored at the cell center like in a collocated arrangement but computations are performed at the cell faces (which was initially proposed by [62]) to prevent checkerboard type errors as well as inconsistent descritization (discussed in [21,50]). The Finite Volume Method is employed to solve the governing equations with spatial and temporal terms discretized based on Table 1. The discretized governing equations are solved with iterative solvers with the relevant preconditioners/smoothers tabulated in Table 2. The maximum number of iterations is set such that the solution of flow variable converges and satisfies the tolerance criterion defined in Table 2. A summary of the parameters used in the solution algorithm is provided in Table 3. Unless otherwise noted, the time step taken by the proposed solver is based on the maximum Courant number which is set equal to 0.05.

3. Definition of test cases

3.1. Computational domain and boundary conditions

The two-dimensional computational domain used in the simulations is a rectangle, of length (L_e) and height (L_{ac}) equal to 10 mm and 5 mm respectively, as illustrated in Fig. 2. Although the simulations discussed in the paper are two-dimensional, OpenFOAM® requires a finite thickness with a single cell resolution in the third direction, represented by h, which is set to 1 micrometer. These 'additional' boundaries are set to 'empty' boundary conditions to perform a 2D simulation. The area of each electrode, A, is computed as $L_e \times h$ and the volume of the entire domain is equal to $A \times L_{ac}$. The left and right boundaries are assigned zero gradient for volume fraction of liquid (α_1), dissolved gas concentration (C_i), local mass transfer rate (ψ) and electrical potential (Φ) where as single field velocity ($\vec{U}$) and modified pressure (p_{rgh}) are set as inletOutlet (zero gradient for outflow but back flow into the domain is restricted by setting zero velocity) and fixed value (equal to 0 Pa)

Table 3
Summary of the other settings used in the solution algorithm.

Parameter	Value	Notes
nAlphaCorr	2	Number of α_1 correction [27].
nAlphaSubCycles	1	Number of sub-cycles of α_1 equation within each time step [61].
cAlpha (C_α)	1	Used for interface compression in Eq. 21 [21,61].
MULESCorr	yes	Switches on semi-implicit MULES [58].
nLimiterIter	3	Number of MULES iterations over the limiter [58].
momentumPredictor	no	Controls solving of the momentum predictor [61].
nOuterCorrectors	1	PISO algorithm is selected by setting this parameter equal to unity in PIMPLE algorithm [61].
nCorrectors	3	The number of times the PISO algorithm solves the pressure and momentum equation in each time step [61].
nNonOrthogonalCorrectors	0	Used when meshes are non-orthogonal [61].
relaxationFactors	1	Specifies the under-relaxation factors used for fields and equations, see [25].
C_{sh}	0.3	Sharpening coefficient used in Eq. 11: set to enable simulation of a sub-millimeter bubble, see [26,27].
$D\Delta t$	10^{-6}	Smearing of the local mass transfer rate (based on sensitivity studies performed in [27]).
He_i	10^{-4}	Concentration jump across interface, used in Eq. 13: set to simulate dissolved gas, see parametric study in [27].
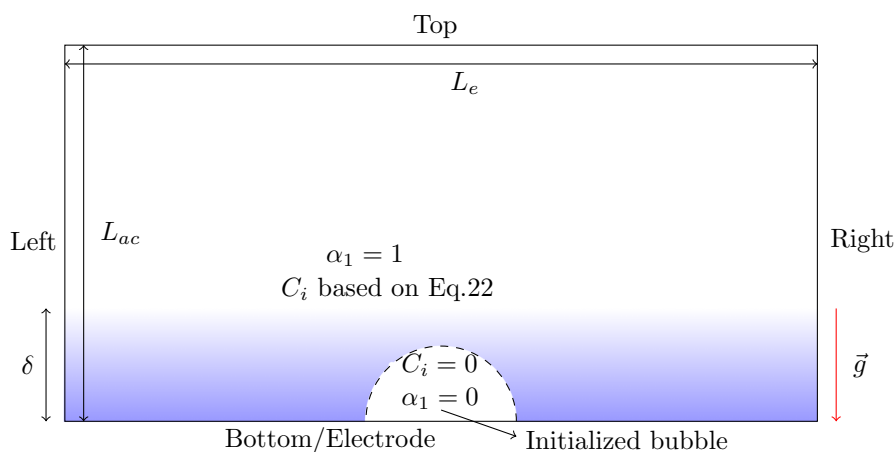
Fig. 2. Illustration of computational domain used in the simulations and the initial conditions used in the simulations.

respectively. The top boundary is assigned zero gradient for α_1, fixed value (equal to 0 mol/m³) for C_i, fixed value (of 0.2 V) for electrical potential (Φ), fixedFluxPressure for p_{rgh}, zero gradient for ψ and no-slip for velocity. The bottom boundary, referred to as electrode, is assigned zero gradient for α_1 along with the static contact angle (θ) condition at the electrode, fixed gradient (which is computed based on Faraday's law of electrolysis[1]) for the dissolved gas concentration (C_i), fixed value (of 0.0 V) for Φ, fixedFluxPressure for modified pressure, zero gradient for ψ and no-slip for velocity. The boundary conditions of electrical potential (Φ) are chosen such that the current density obtained from the system when bubbles are not present in the domain is calculated from Ohm's law, as $\kappa_1(\Phi_{top} - \Phi_{electrode})/L_{ac}$, to be equal to 1210.8 A/m² which is in the practical range (between 1000–3000 A/m²) used in commercially used alkaline electrolyzer systems, see [63].

As C_i indicates the concentration of the dissolved gas which exceeds the saturation condition, which for hydrogen dissolved in water under 1 atm and 25 °C is 0.79 mol/m³ [64], the concentration boundary layer at the electrode is initialized based on the vertical distance from the electrode (y), as shown in Fig. 2, such that

$$C_i = \begin{cases} C_{i,y=\delta} \text{ (when } y > \delta), \\ C_{i,y=0} + (C_{i,y=\delta} - C_{i,y=0})y/\delta \text{ (when } y \leq \delta), \end{cases} \qquad (22)$$

where δ is the concentration boundary layer thickness set to 0.5 mm (see Appendix E), $C_{i,y=0}$ and $C_{i,y=\delta}$ is the concentration at the electrode and distance of δ (or larger) which is set equal to 125.66 mol/m³ (based on supersaturation reported in [65]) and 0 mol/m³ (which corresponds to saturation) respectively. It should be noted that the initialized concentration boundary layer does not account for the depleted concentration of the dissolved gas near the bubble due to interfacial mass

---

[1] The boundary condition for C_i at the electrode, which is computed based on Faraday's law of electrolysis, is $\partial_n C_i = |\vec{i}|\alpha_1/(nFD_{i,1})$, where n is the number of electrons transferred for the electrochemical reaction to produce hydrogen (equal to 2), F is the Faraday's constant (equal to 96,485 As/mol) and $D_{i,1}$ is the diffusion coefficient of dissolved hydrogen in the liquid.

Table 4

The fluid properties, based on 1atm and 25 °C, for Phase 1 (liquid/electrolyte) and Phase 2 (hydrogen bubble) used in the simulations.

Properties	Dimensions	Phase 1	Phase 2
Density (ρ)	kg/m^3	1075.05	0.082
Viscosity (ν)	m^2/s	9.89×10^{-7}	0.00011
Diffusion coefficient (D_i)	m^2/s	4.80×10^{-9}	1×10^{-5}
Electrical conductivity (Γ)	S/m	30.27	1×10^{-13}
Molar mass (M_i)	kg/mol	2×10^{-3}	
Surface tension (σ)	N/m	0.072	

transfer across the interface. The single bubble in the domain, which is initialized as in Fig. 2, is located such that its center is 5 mm from the left boundary and 0 mm from the bottom boundary (y_c). In the case of two bubbles, used in coalescence studies, with radii equal to R_{2a} and R_{2b}, the bubbles are initialized as semicircles such that the centers of the bubbles are a distance of $5 \times 10^{-3} - R_{2a}$ and $5 \times 10^{-3} + R_{2b}$ from the left boundary. As the electrodes are horizontal with respect to gravity, which is set as $|\vec{g}| = 9.81$ m^2/s, the evolution of the bubble would lead to detachment and subsequent vertical rise due to buoyancy. The fluid properties used in the simulations is described in Table 4. The computational geometry is meshed by 1600×800 hexahedral cells based on the mesh convergence study in described in Appendix C.

3.2. Definition of parameters

Although visual comparison is a very useful tools to interpret the results, to compare various simulations and quantify its results, it is important and easier to use standardized parameters. The standardized parameters which are used in the paper for analyzing the results are defined in this section.

Normalized bubble volume, The volume of the bubble at any time (V) is calculated as $\int \alpha_2 dV$ and the corresponding area of the bubble is equal to V/h, where h is unit cell thickness. The normalized bubble volume is calculated as the fraction of the computational domain occupied by the bubble (f) which is determined as

$$f = \frac{V}{A \times L_{ac}} \tag{23}$$

where A is the area of the electrode and L_{ac} is the inter-electrode distance. For the geometry used in the simulation $A \times L_{ac}$ is equal to 5×10^{-11} m^{-3}, see Fig. 2.

Rise velocity. The mean velocity with which a bubble rises is computed as

$$U_{rise} = \frac{\int \vec{v} \alpha_2 dV}{\int \alpha_2 dV} \tag{24}$$

where $\vec{v}$ is the vertical component of the velocity vector. The rise velocity, computed based on Eq. 24, has been been previously used in works like [66] and [25] to study the dynamics of single rising bubble.

Bubble coverage of electrode. The fraction of the area of the electrode covered by the bubble is computed as

$$\Theta = \frac{\sum \alpha_2 |\vec{S}|}{\sum |\vec{S}|}, \tag{25}$$

which is computed at the electrode boundary with $|\vec{S}|$ representing the magnitude of the surface area of the individual mesh cell at the boundary and $\sum |\vec{S}|$ is the area of the electrode (A), which is equal to 10^{-8} m^2. The fraction of the electrode area in contact with the electrolyte is equal to $1 - \Theta$. When the bubble has detached or when the whole electrode is in contact with the electrolyte, Θ reduces to zero.

Bubble detachment. Based on the temporal variation of $1 - \Theta$, the bubble is considered to have detached when $1 - \Theta > 0.999$ and the corresponding time, which is indicated by τ_d, is considered as the detachment time of the bubble.

Average current. As the proposed solver computes local current density ($\vec{i}$), the current obtained from the system (I) is equal to

$$I = \sum \vec{i} \cdot \vec{S}, \tag{26}$$

which is the sum of dot product of local value of current density and cell area vector of individual mesh at the electrode boundary. For simplicity, a normalized average current (I/I_0) is used in this paper which is determined as the ratio of I to I_0 which is the current obtained when bubbles are absent in the system.[2]

Bubble deformation. As the bubble detaches from the surface, it undergoes deformation which is measured horizontally (Δx) and vertically (Δy). The horizontal deformation of the bubble at any time step is calculated as the difference between

---

[2] Theoretically the current which can be obtained for the applied potential difference is when the system does not have any bubbles can be calculated by substituting relevant values in $I_0 = \Gamma_1 A (\Phi_{topboundary} - \Phi_{electrode})/L_{ac}$ which gives I_0 equal to 1.2108×10^{-5}A.
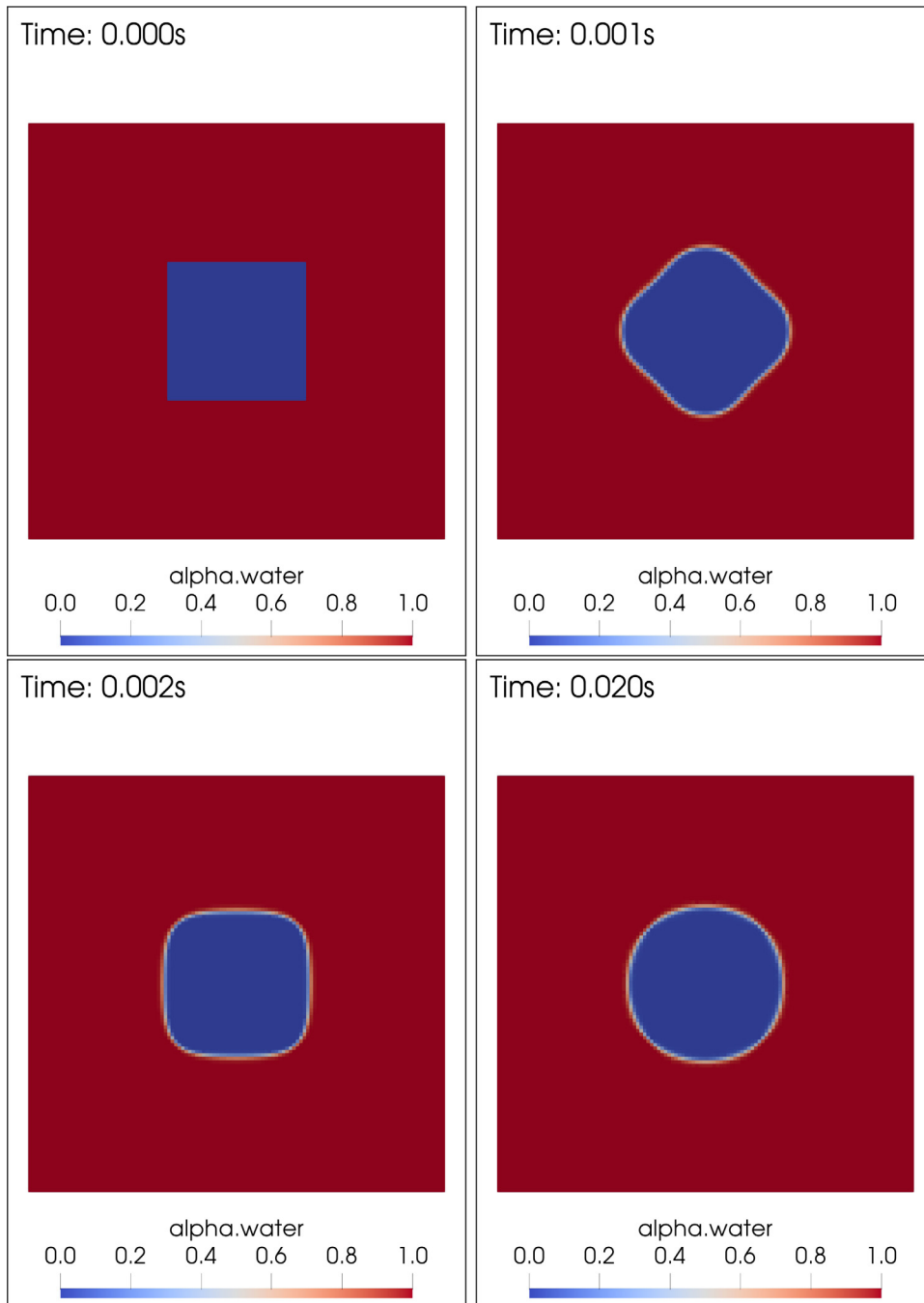
Fig. 3. Temporal change in α_1 as initialized square bubble reaches the equilibrium shape i.e. a stationary circular bubble..

maximum and minimum x coordinates of the interface ($\alpha_1 = 0.5$). Similarly Δy is the difference between maximum and minimum y coordinates of the interface.

4. Verification of the proposed solver

In this work, the proposed solver is verified in a modularized manner which allows for sequential verification of parts of the proposed solver with existing analytical and computational benchmarks. The benchmarks used in this work are based on static 2D bubble, dynamic case of rising 2D bubbles, growth of 2D bubble driven by supersaturation and qualitative assessment of the variation of current. Apart from these verification cases, the relevant imbalance (mass of liquid/bubble
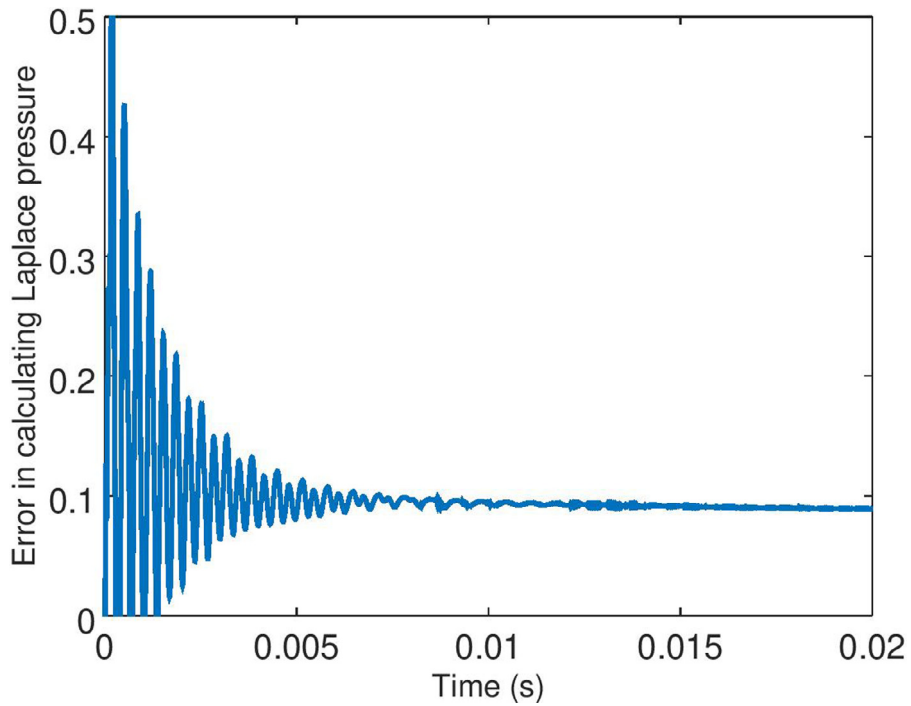
Fig. 4. Temporal change in the error in calculating the Laplace pressure, calculated as $\frac{\Delta p_c - \Delta p}{\Delta p_c}$ where Δp_c is determined based on Eq. 27, $\Delta p = \frac{\int \alpha_2 \, p \, dV}{\int \alpha_2 \, dV} - p_0$ and p_0 is the operating pressure used in the simulation (equal to 0 Pa)..
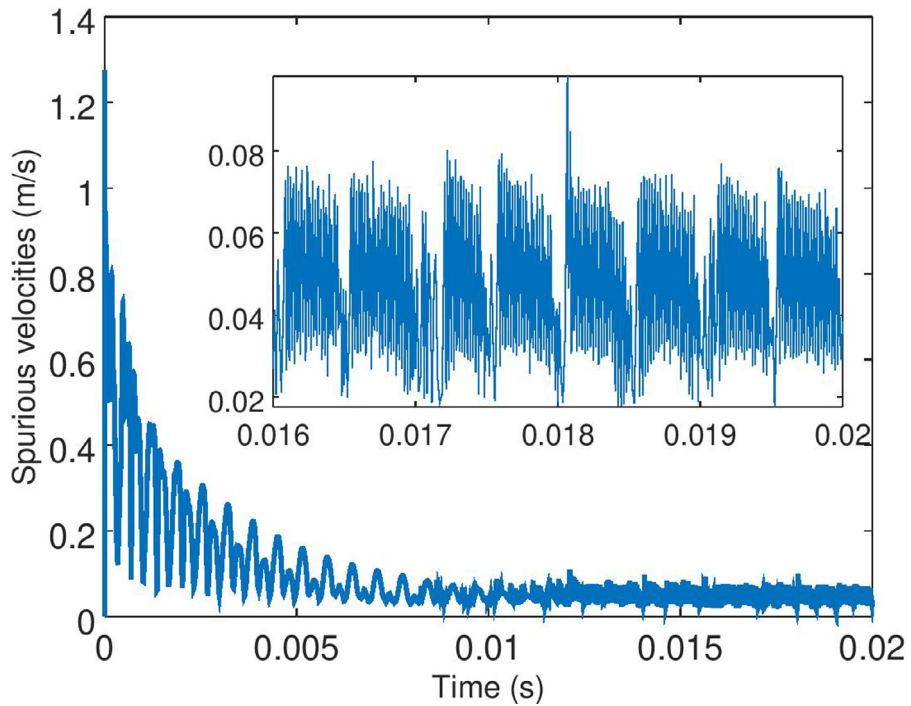
Fig. 5. Evolution of spurious velocities, calculated as $\max(|\vec{U}|)$, during stationary bubble simulation..
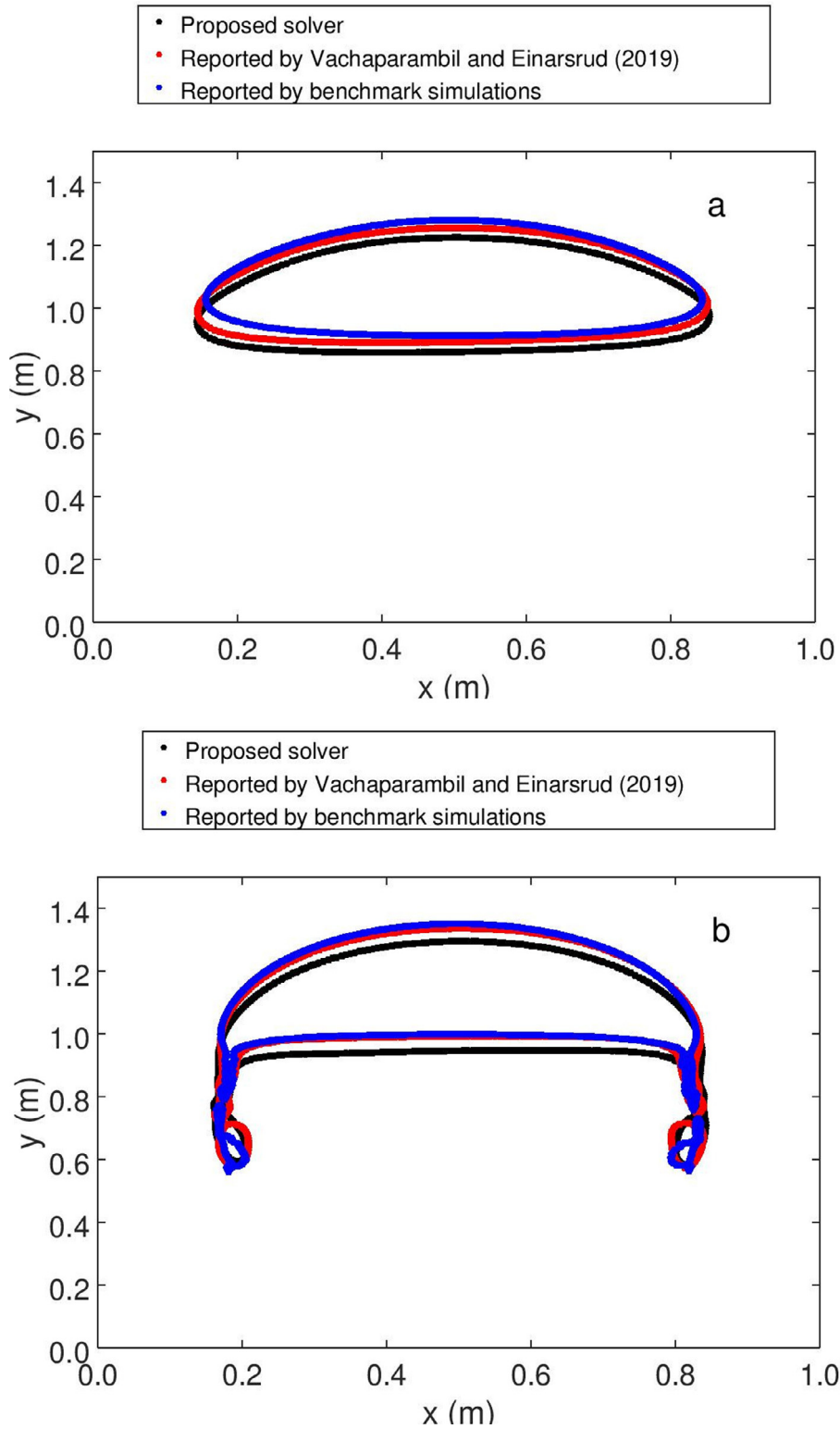
Fig. 6. Comparison of bubble morphology at $t = 3$ s predicted by the solver and results reported in literature[25,66]: a) TC1 b) TC2. The data used for comparison are obtained from benchmark simulations of [66] and our previous work [25].
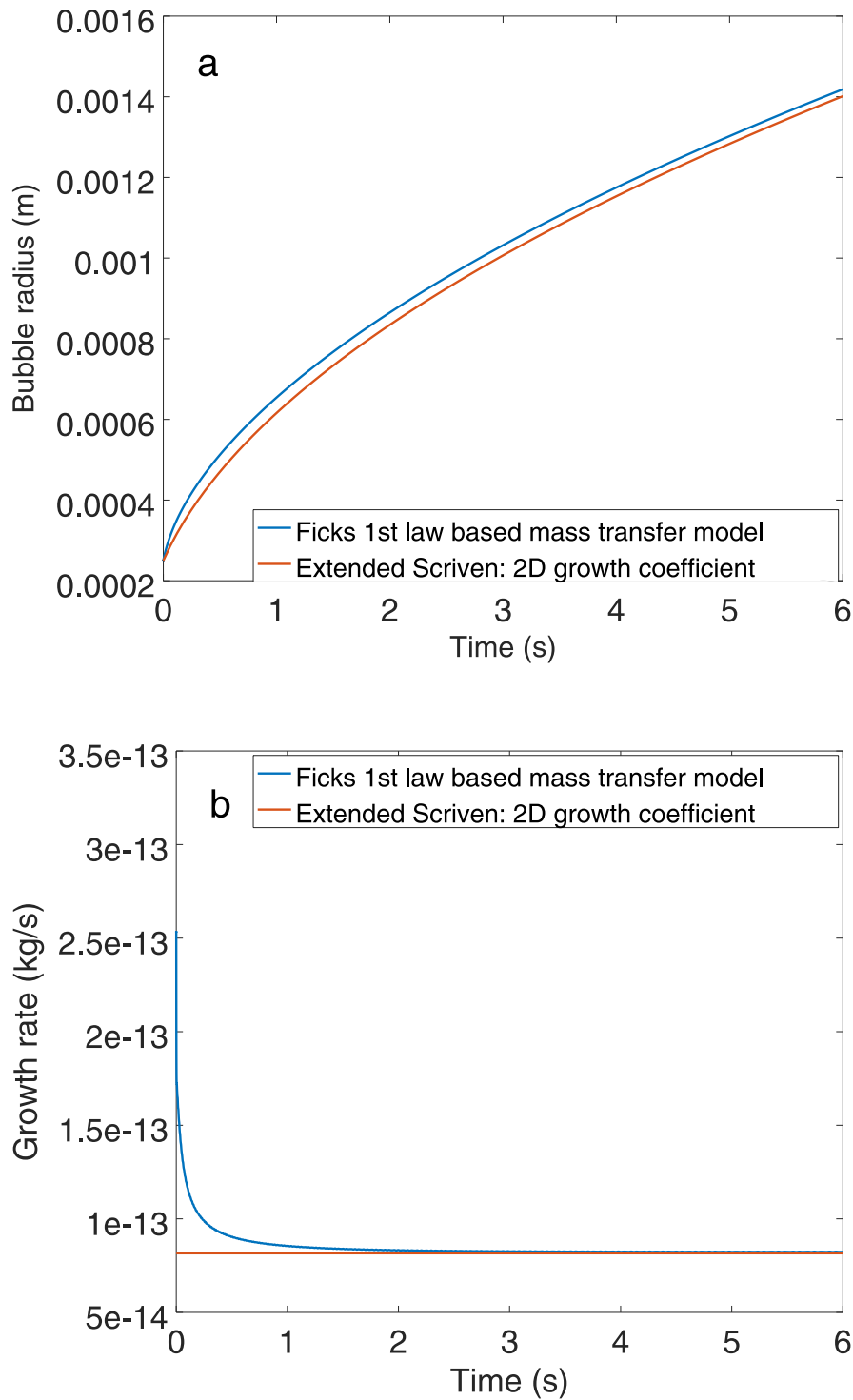
Fig. 7. Comparison of the prediction of the proposed solver with the Extended Scriven model to predict the bubble growth from a pre-existing bubble in a uniformly supersaturated solution: a) Bubble radius b) Growth rate.
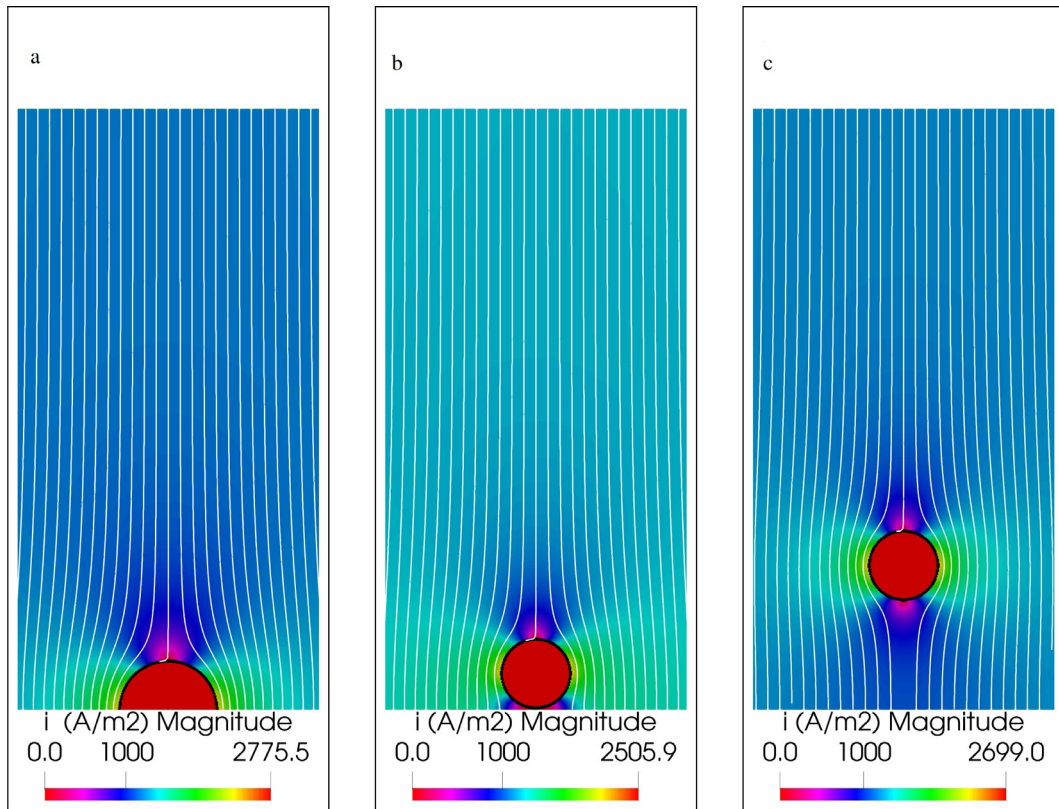
Fig. 8. The distribution of $|\vec{i}|$ for static bubble simulations: a) TC1a b) TC2a and c) TC2d. The white lines represents the current lines in the liquid phase whereas the black line indicates the interface (i.e. $\alpha_1 = 0.5$)..
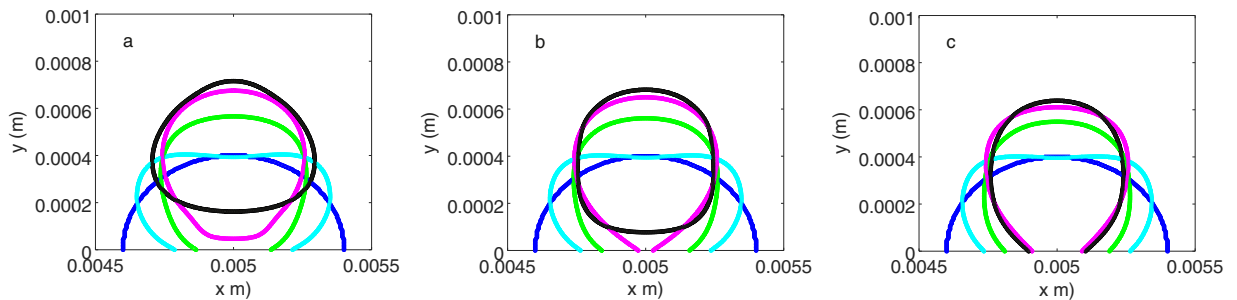
Fig. 9. The evolution of the bubble (isosurface of $\alpha_1 = 0.5$) at 0s (——), 5×10^{-4}s(——), 1×10^{-3}s(——), 1.5×10^{-3}s(——) and 2×10^{-3}s(——) for the various wetting condition at the electrode: (a) 15° in SCT0, (b) 30° in SCT1, and (c) 45° in SCT2.

and dissolved gas), mesh and temporal convergence studies have also been performed in Appendix B, Appendix C and Appendix D respectively.

4.1. Stationary bubble

The first step in the verification of the proposed solver is based on the ability to simulate evolution of the 2D square bubble, initialized in the computational domain, which due to surface tension (and absence of gravity) reaches the equilibrium shape i.e. a stationary circular bubble. At equilibrium, the Laplace pressure of the 2D bubble can be calculated analytically using the Young-Laplace equation as

$$\Delta p_c = \frac{\sigma}{R}, \tag{27}$$

where σ is the surface tension and R is the 2D bubble radius. Additionally, at equilibrium, the velocities in the domain should theoretically reduce to zero.
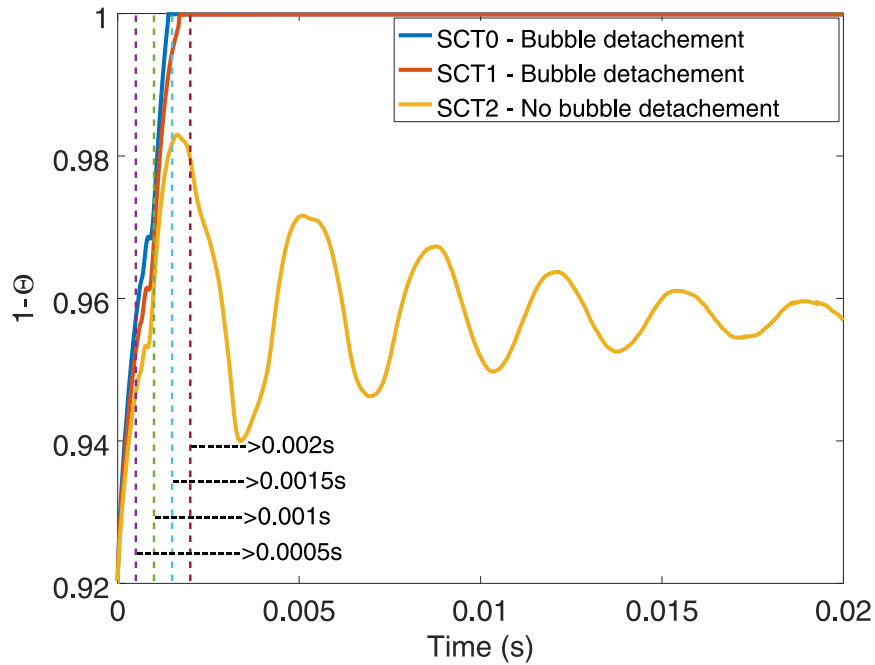
Fig. 10. Temporal change in the fraction of area of the electrode in contact with the electrolyte $(1 - \Theta)$ as the bubble evolves in SCT0 ($\theta = 15°$), SCT1 ($\theta = 30°$) and SCT2 ($\theta = 45°$). The timesteps at which the isosurface of $\alpha_1 = 0.5$ is extracted to plot Fig. 9 is illustrated using vertical dashed lines.
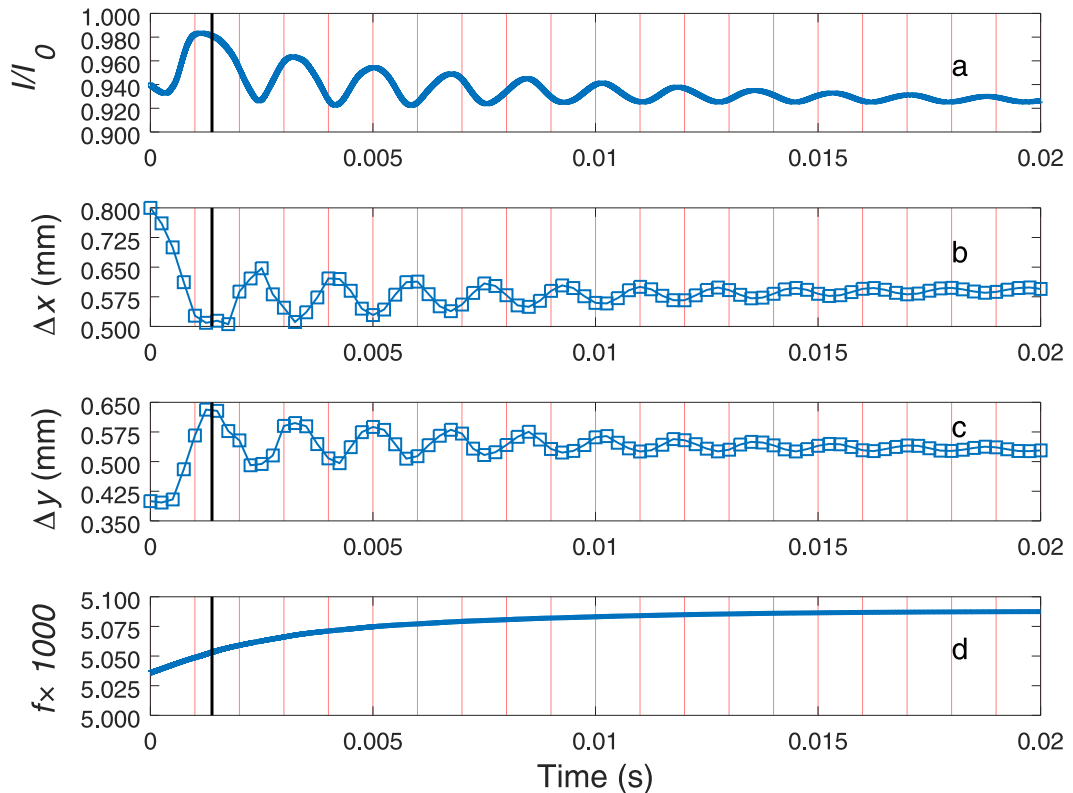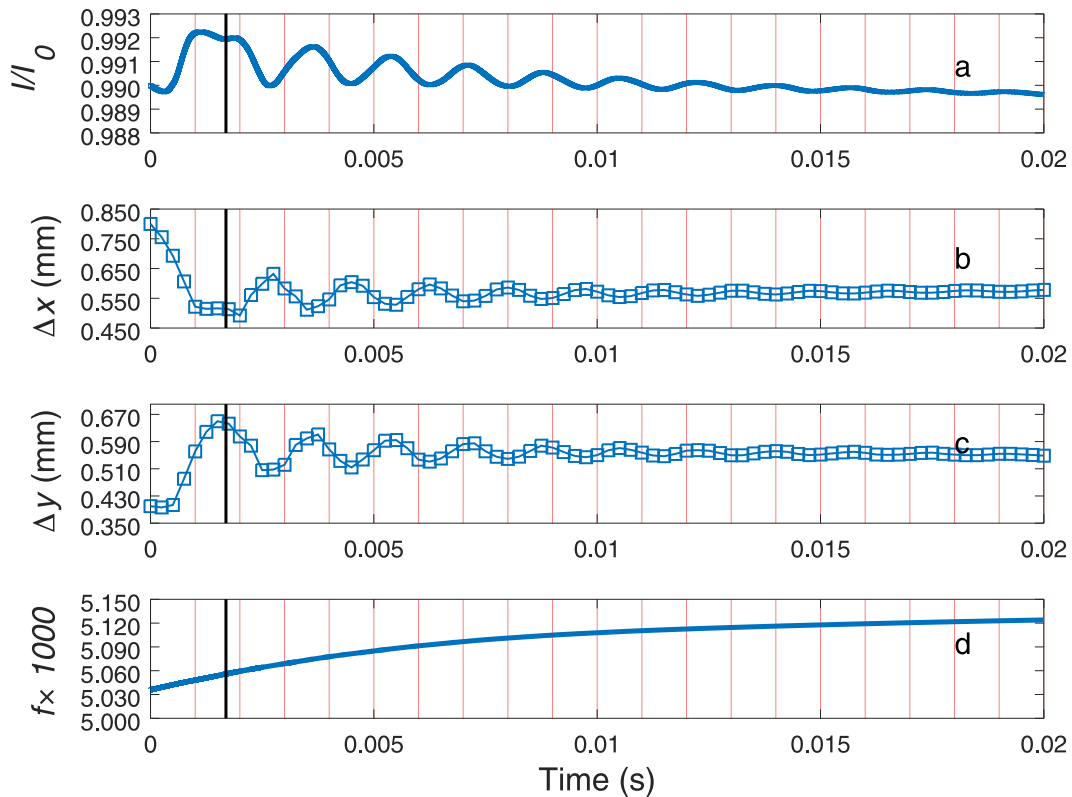

Fig. 11. The temporal variation of various relevant parameters during bubble detachment in SCT0 ($\theta = 15°$): a) normalized current (I/I_0), b) horizontal deformation (Δx), c) vertical deformation (Δy), d) normalized volume of bubble (f). The vertical black line indicates the detachment time, τ_d, and the vertical red lines are equidistant grid line at every 0.001s to enable comparison between the plots.

Fig. 12. The temporal variation of various relevant parameters during bubble detachment in SCT1 ($\theta = 30°$): a) normalized current (I/I_0), b) horizontal deformation (Δx), c) vertical deformation (Δy), d) normalized volume of bubble (f). The vertical black line indicates the detachment time, τ_d, and the vertical red lines are equidistant grid line at every 0.001s to enable comparison between the plots.

In order to simulate the above mentioned flow scenario, gas is initialized as a square region (equal to 0.6×0.6 mm^2) in the center of the computational domain (of dimensions 1.8×1.8 mm^2). The fluid properties used for the simulations is described in Table 4 with the exception of gravity which is set to zero. The boundary conditions used for α_1, ψ and $\vec{U}$ are zero gradient where p_{rgh} uses a fixed value (equal to 0 Pa) on all four boundaries. C_i uses fixed value (equal to 0 mol/m^3) on the top boundary and zero gradient on the remaining three boundaries. For Φ, the left and right boundaries are assigned fixed value (equal to 0 V) and other boundaries are set to be zero gradient. The computational domain is meshed with 120×120 cells. Theoretically, the radius of circle (which has the same area as the initialized square) is 338.6 micrometers and the corresponding Laplace pressure, calculated using Eq. 27, is equal to 212.64 Pa.

The evolution of the bubble from the initialized square to the equilibrium circular shape is shown in Fig. 3. As the bubble reaches equilibrium, the Laplace pressure obtained from the simulation also reaches ready a constant value, see Fig. 4. At $t = 0.02$ s, the Laplace pressure obtained from the simulations has an absolute error of around 9% with respect to the corresponding analytical solution, which is similar to errors reported in works like [25,26]. Although the bubble reached the equilibrium shape, the existence of spurious velocities, which arise from errors in estimating the interfacial curvature (see Appendix A), causes a non-zero velocities in the computational domain which has been shown in Fig. 5.

4.2. Rising bubble

The next verification case used in this paper is based on the work by [66], who proposed computational benchmark for two 2D rising bubbles which has been extensively used in literature, like [25,30,31]. The work by [66] reported the bubble morphology, rise velocities and circularity for two rising bubble scenarios (which differ based on the Capillary number) using codes like TP2D, FreeLIFE and MoonNMD. In this paper, verification of the proposed solver is based on bubble morphology reported by the original work of [66] using FreeLIFE code and [25] who performed these rising bubble simulations using VOF solver in OpenFOAM® with surface tension modelled using the Sharp Surface Force model.

The simulations use a computational domain of dimensions 1×2 m^2 where a bubble of diameter equal to 0.5 m is initialized such that its center is half a meter from the bottom boundary and equidistant from the side walls. The computational domain is meshed using 160×320 cells, see [25,30,31,66]. It should be pointed out that fluid properties like density, viscosity, acceleration due to gravity and surface tension are set based on [25,66] but the remaining parameters are
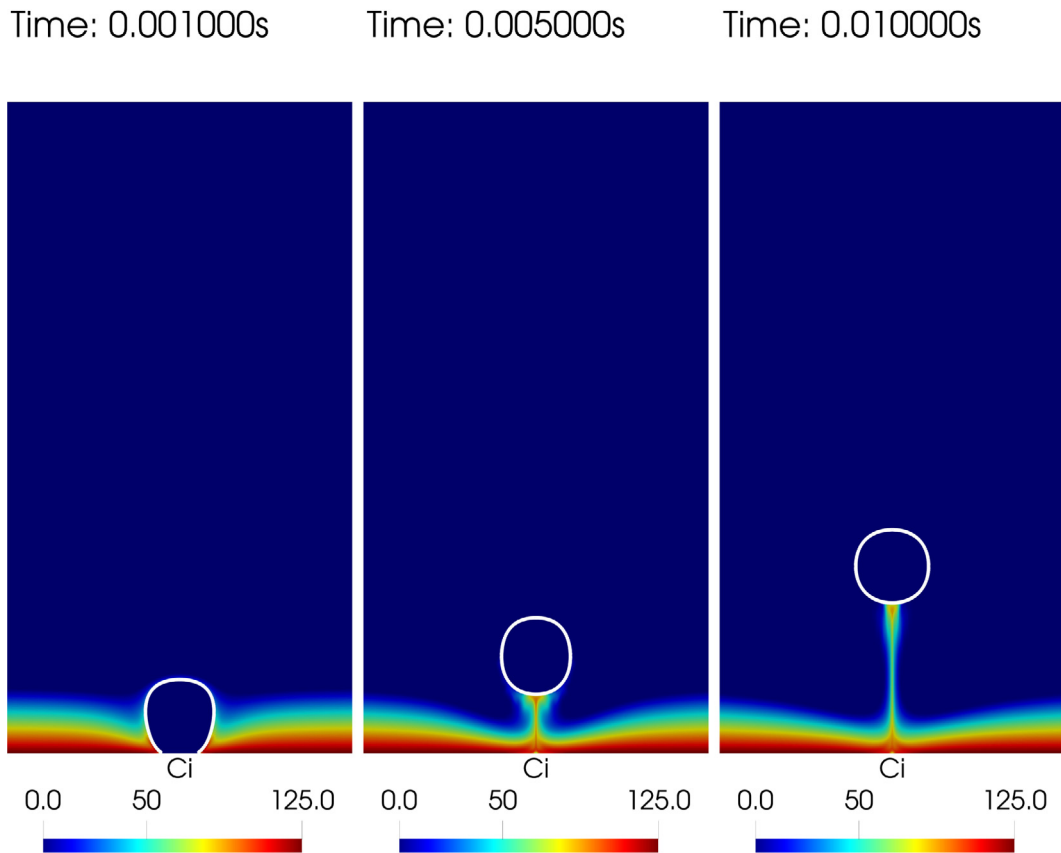
Fig. 13. The change in the dissolved hydrogen concentration (mol/m^3) as the bubble evolves in the case of SCT0. The white line represents the interface which is plotted at $\alpha_1 = 0.5$. See supplementary materials for more information.

set equal to values described in Table 4. The two rising bubble cases can be differentiated based on the relevant Capillary number (Ca)

$$Ca = \frac{\rho_1 \nu_1 U_g}{\sigma}, \tag{28}$$

where U_g is equal to $\sqrt{|\vec{g}|L}$ and L is the characteristic length (equal to the diameter of the initialized bubble) [25,31,66]. The two cases, represented by TC1 and TC2, has an associated Ca which is equal to 0.268 and 3.571 respectively. The four boundaries in the domain are set to zero gradient for ψ, α_1 whereas C_i is set to fixed value (equal to 0 mol/m^3) at top boundary and remaining boundaries are set to zero gradient. For p_{rgh}, the top boundary is set to fixed value (equal to 0 mol/m^3) and remaining boundaries are set to zero gradient. For Φ, the top and bottom boundaries are set to zero gradient whereas left and right boundaries are assigned to be fixed value (equal to 0 V). The boundary conditions for $\vec{U}$ are set as no-slip at top and bottom boundaries whereas left and right boundaries are set as slip walls.

The case, TC1, which corresponds to flow with $Ca = 0.268$, as the surface tension effects are dominant the rising bubble deforms to an ellipsoidal shape, see Fig. 6a. On the other hand, TC2 which has a higher Capillary number, i.e. $Ca = 3.571$, (when compared to TC1) results in forming a skirted bubble with filaments along the sides, see Fig. 6b. The final bubble shape in both these cases are obtained at $t = 3$ s and it compared against bubble morphology reported by [66] and [25] in Fig. 6. The predicted bubble morphology for both 2D rising bubble simulations agree reliably with the results from [25,66]. The deviations between the predictions from the proposed solver and the data reported in literature can be attributed to spurious velocities, see discussions in [25,30,31]. It is also worth pointing out that the deviation between the proposed solver and data reported in [25], using the SSF model, can also be attributed to spurious velocities as its evolution is dependent on the maximum time step used, which in the former is based on Courant number (equal to 0.05) whereas the latter used a time step constraint proposed by [21,67]. The effect of time step used in the simulations is further discussed in Appendix D. Another possible reason for variation in the spurious velocities between the present and previous work is the different values of sharpening coefficient which is set equal to 0.3 and 0.5 respectively (Eq. 11), see [26] for discussion on the influence of C_{sh} on these numerical artifacts.
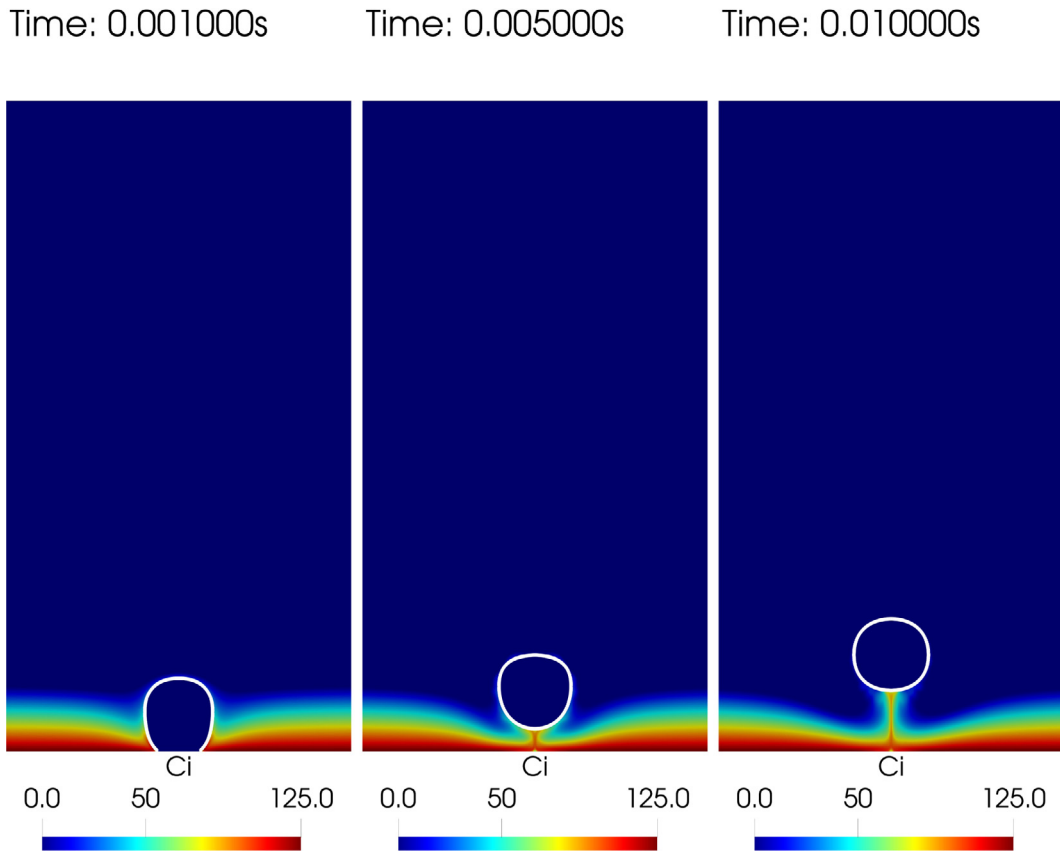
Fig. 14. The change in the dissolved hydrogen concentration (mol/m^3) as the bubble evolves in the case of SCT1. The white line represents the interface which is plotted at $\alpha_1 = 0.5$. See supplementary materials for more information.
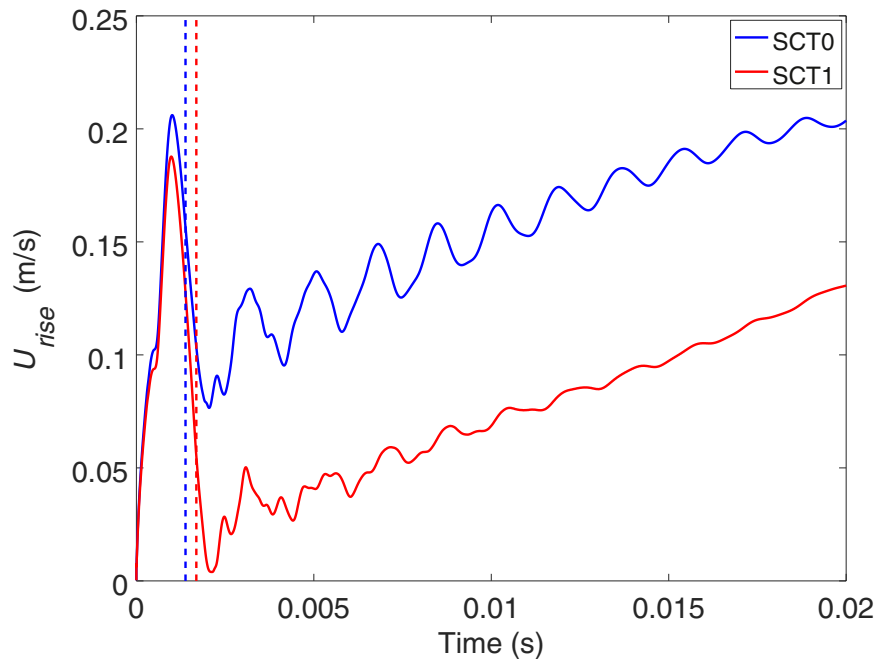

Fig. 15. The temporal variation of the rise velocity for SCT0 ($\theta = 15°$) and SCT1 ($\theta = 30°$) with the detachment time (τ_d) represented using dashed lines (blue for SCT0 and red for SCT1).
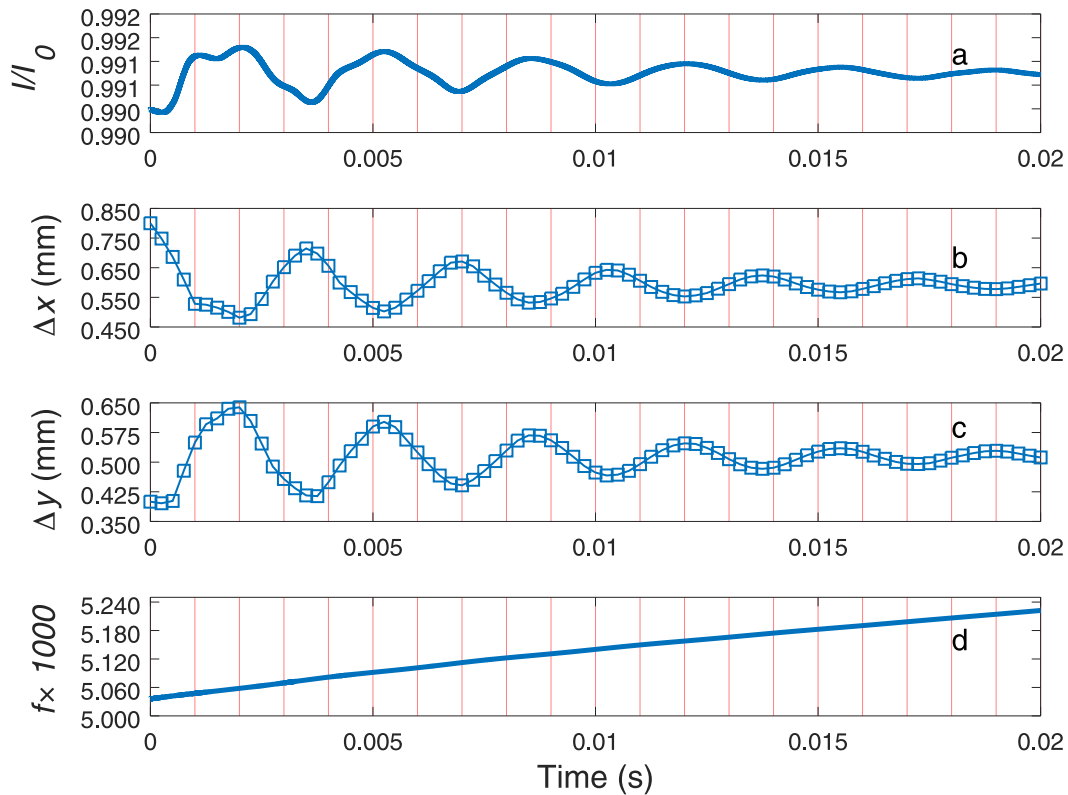
Fig. 16. The temporal variation of a) normalized current (I/I_0), b) horizontal deformation (Δx), c) vertical deformation (Δy), d) normalized volume of bubble (f) for SCT2 ($\theta = 45°$) as the bubble deforms on the electrode surface. The vertical red lines are equidistant grid line at every 0.001s to enable comparison between the plots.

4.3. Bubble growth in a uniformly supersaturated solution

The next step in verifying the proposed solver is based on bubble growth driven by supersaturation. The bubble growth predicted by the proposed solver is set up using the domain, boundary and initial conditions along with the mesh is set as described in [27] with the exception of Φ which uses fixed value (equal to 0 V) at left and right boundaries but the remaining boundaries are set as zero gradient condition. The fluid properties as well as the solution algorithm is based on details summarized in Table 3 and Table 4 but both gravity and surface tension effects are ignored. The computational setup describes the growth of hydrogen bubble, with radius equal to 0.25 mm, due to the uniform supersaturation of 200.64 mol/m³ in an unbounded medium. Due to low solubility of hydrogen in water, this initialized uniform dissolved gas corresponds to a supersaturation equal to $200.64/0.79 \approx 254$. It should be noted that the small values of supersaturation reduces the driving force for interfacial mass transfer which results in a smaller bubble, see [34]. This setup allows for the verification of the result with exact analytical results which was earlier derived by [68] as an extension of the phenomenological work by Scriven [69] to account for the size of the pre-existing bubble at $t = 0$ s. The evolution the bubble radius as it grows due to interfacial mass transfer is described by Extended Scriven model as

$$R_{ext-scriven} = 2\beta \sqrt{D_{i,1}\left(t + \frac{R_0^2}{4D_{i,1}\beta^2}\right)}, \qquad (29)$$

where β is the growth coefficient which was proposed by [69] and R_0 is the radius of the bubble at $t = 0$ s. The growth coefficient for 2D bubbles in a uniformly supersaturated unbounded solution, derived in [27], is given by

$$\beta_{2D} = \frac{a + \sqrt{a^2 + 4a}}{2\sqrt{2}}, \qquad (30)$$

where a is calculated as

$$a = \frac{M_i \Delta C}{\rho_2}, \qquad (31)$$

where ΔC is the difference between the bulk concentration of the dissolved gas and the saturation concentration at the interface, equal to 200.64 mol/m³ for this case. The radius predicted by the proposed solved is calculated as $R = \sqrt{V/(\pi h)}$
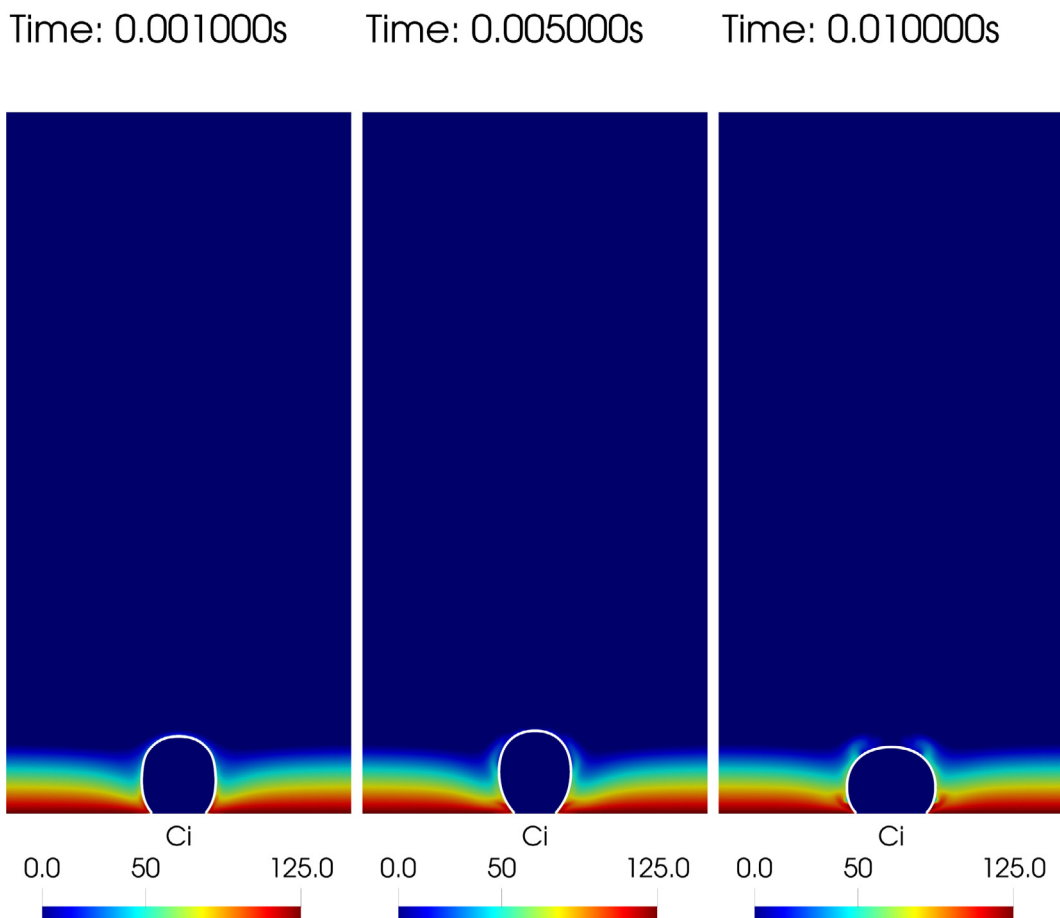
Fig. 17. The change in the dissolved hydrogen concentration (mol/m^3) as the bubble evolves in the case of SCT2. The white line represents the interface which is plotted at $\alpha_1 = 0.5$. See supplementary materials for more information..

where V is defined as in Eq. 23 and growth rate is computed as $\int \psi_0 dV$. The bubble radius and growth rate predicted by the proposed solver and the analytical solution is compared in Fig. 7. The small discrepancy between the bubble radius predicted by the simulation and analytical solution is the result of the lack on concentration boundary layer around the interface in the initialized C_i used in the simulation which causes growth rate which is larger than the corresponding analytical value. This larger growth rate occurs till the concentration boundary layer is established and phenomena becomes diffusion limited, see [27,34].

4.4. Effect of the bubble on current

The current in a pure electrolyte between two parallel electrodes has vertical path lines. As the bubbles are non-conductive, the current path lines are deformed in its vicinity which causes the increase in resistance and decrease in current under constant potential difference [38]. In a homogeneous medium, the overall resistance is directly proportional to the l/A where l is the characteristic length which is equal to L_{ac} when bubbles are absent in the system. When a bubble is present in the bulk of the electrolyte, the increased resistance is a result of the deformed the path lines of current which cause an increase in l. Similarly, when bubble is present on the electrode, the electrode-electrolyte area is reduced to $A(1 - \Theta)$ which results in larger resistance (if l is constant), than when the bubble is in the bulk. Experimental works, like [70], reported a decrease in current as the bubble grows on the electrode and an increase when the bubble has detached. In this last verification step, which is qualitative in nature, the ability of the proposed solver to predict the variation of current with bubble evolution is analyzed.

In order to showcase the variations in current, fourteen simplified cases with stationary circular (in bulk) and semicircular (on surface) bubbles are investigated. These simulations differ in the initial conditions of α_1, which are summarized in Table 5. Except for the case of TC1c, which has two bubbles on the surface hence two coordinates for the centers, all other cases have a single bubble. All the boundaries are treated as described in Section. 3.1 with the exception of electrochemical reaction at the electrode which is replaced with a zero gradient condition to prevent addition of dissolved hydrogen to the
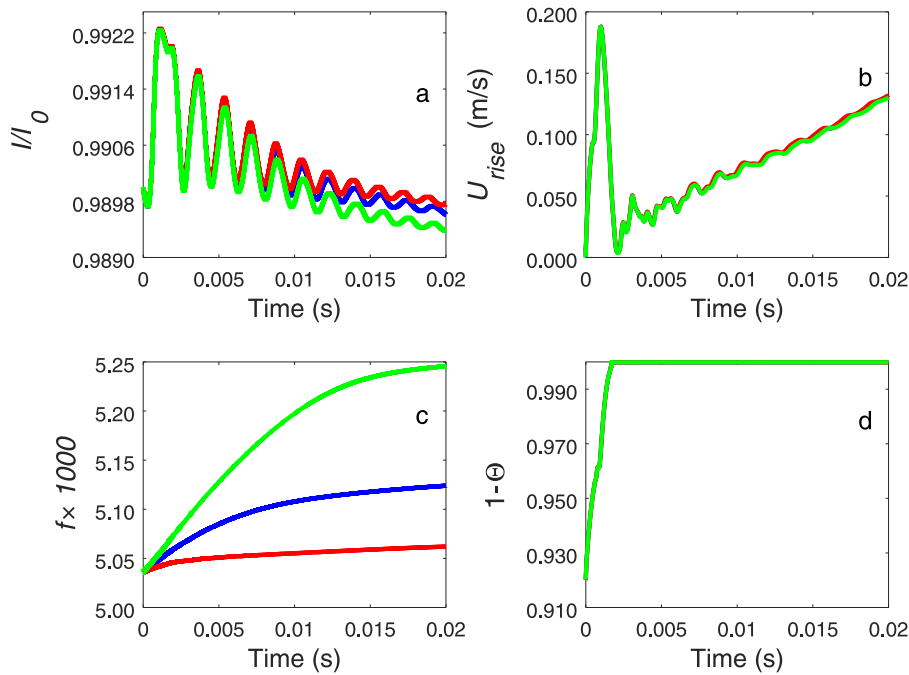
Fig. 18. Comparison of a) I/I_0, b) rise velocity and c) normalized bubble volume (f), d) $1 - \Theta$ obtained for bubble evolution with a contact angle at the electrode set at 30° but the initialized concentration boundary layer thickness is varied from SCT1BL- ($\delta = 0.3$mm indicated with ▬▬), SCT1 ($\delta = 0.5$mm indicated with ▬▬) and SCT1BL+ ($\delta = 0.8$mm indicated with ▬▬).

Table 5
The variation of normalised current (I/I_0) for various static bubble simulations with positions of the center of the bubble denoted by x_c and y_c.

Case	x_c (m)	y_c (m)	f	Δx (mm)	Δy (mm)	$1 - \Theta$	I/I_0
TC1a	0.0050	0.0000	0.0051	0.813	0.406	0.92	0.98978
TC1b	0.0050	0.0000	0.0026	0.575	0.288	0.94	0.99487
TC1c	0.0053, 0.0047	0.0000,0.0000	0.0051	1.138	0.288	0.89	0.98329
TC2a	0.0050	0.0003	0.0051	0.575	0.575	1.00	0.99148
TC2b	0.0050	0.0006	0.0051	0.575	0.575	1.00	0.99032
TC2c	0.0050	0.0009	0.0051	0.575	0.575	1.00	0.99002
TC2d	0.0050	0.0012	0.0051	0.575	0.575	1.00	0.98992
TC2e	0.0050	0.0015	0.0051	0.575	0.575	1.00	0.98987
TC2f	0.0050	0.0018	0.0051	0.575	0.575	1.00	0.98985
TC2g	0.0050	0.0021	0.0051	0.575	0.575	1.00	0.98983
TC2h	0.0050	0.0024	0.0051	0.575	0.575	1.00	0.98983
TC3a	0.0050	0.0017	0.0051	0.575	0.575	1.00	0.98986
TC3b	0.0050	0.0017	0.0051	0.578	0.549	1.00	0.98961
TC3c	0.0050	0.0017	0.0102	0.813	0.813	1.00	0.98003

electrolyte which can result in bubble growth. Additionally, both surface tension and gravitational forces are neglected in these simplified simulations to ensure stationary bubbles.

The variation of the current (I/I_0) when bubbles is present in the bulk, the smaller bubbles would indicate lesser distortion of the current path lines (giving a smaller value of l) which results in larger current (I/I_0). This is observed in TC3a when compared to TC3c, see Table 5. When the bubble is horizontally deformed, which is indicated by larger Δx and smaller vertical deformation (Δy), when compared to TC3a, the current path lines are further distorted as a result of the larger projected area of the bubble which reduces the current, as observed in TC3b. Interestingly, current increases closer the detached bubble is to the electrode but it reaches an asymptotic value near half of the inter-electrode distance, as observed in cases TC2a-h. This dependence of current on the location of bubble can be understood as the reduction of the effective distance traversed by the current path lines (l) when the detached bubble is close to the electrode and shields a part of the electrode as deformed current path lines extends for several bubble radii [38], as seen in Fig. 8.

When the bubble is attached to the electrode, in TC1a and TC1b, increase in the bubble footprint is observed to reduce the current as result of the covering the electrode (represented by $A(1 - \Theta)$) and deforming the current path lines which has been observed in experiments like [70]. For the same equivalent volume of bubble, the presence of two bubbles, in
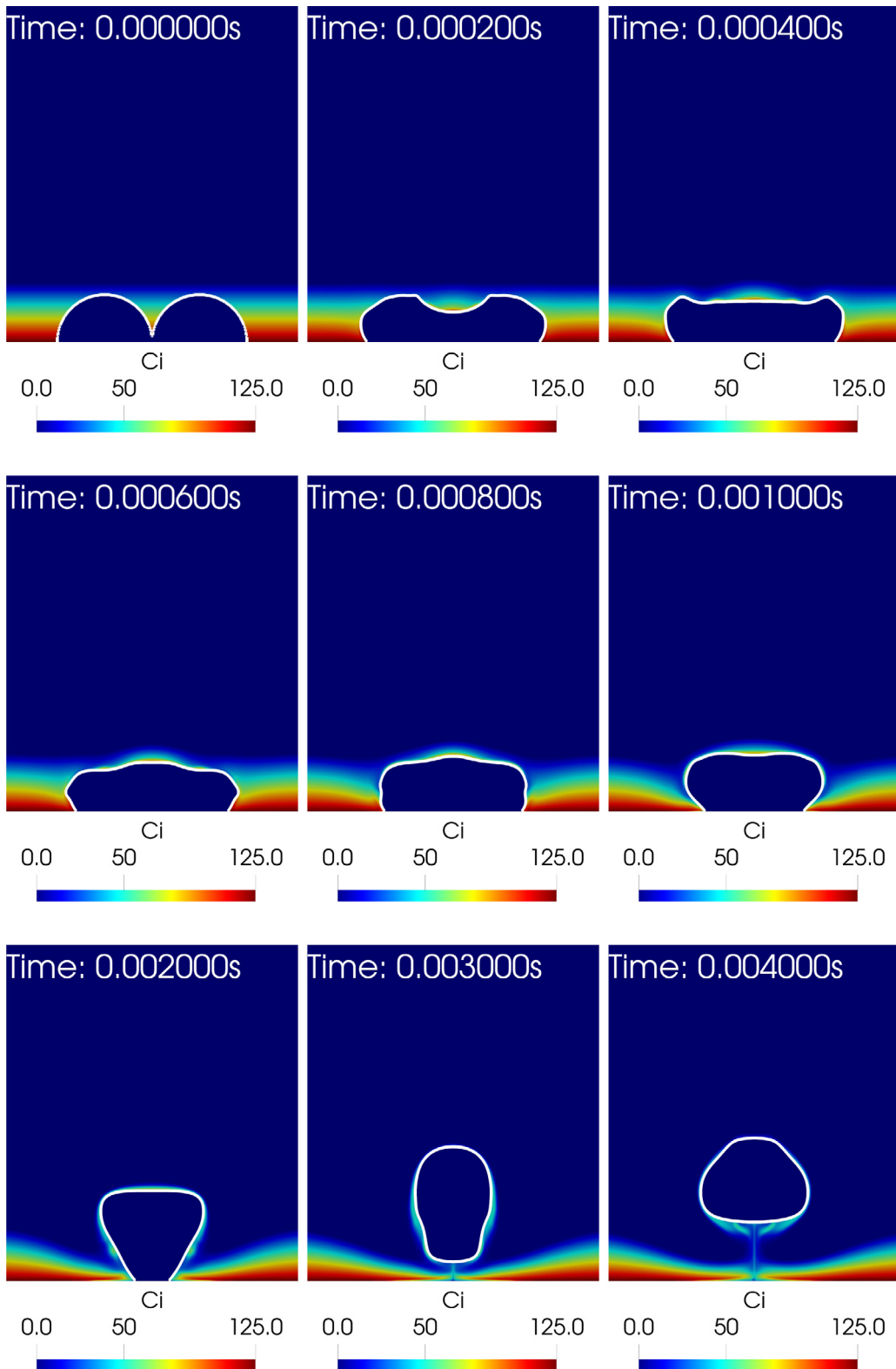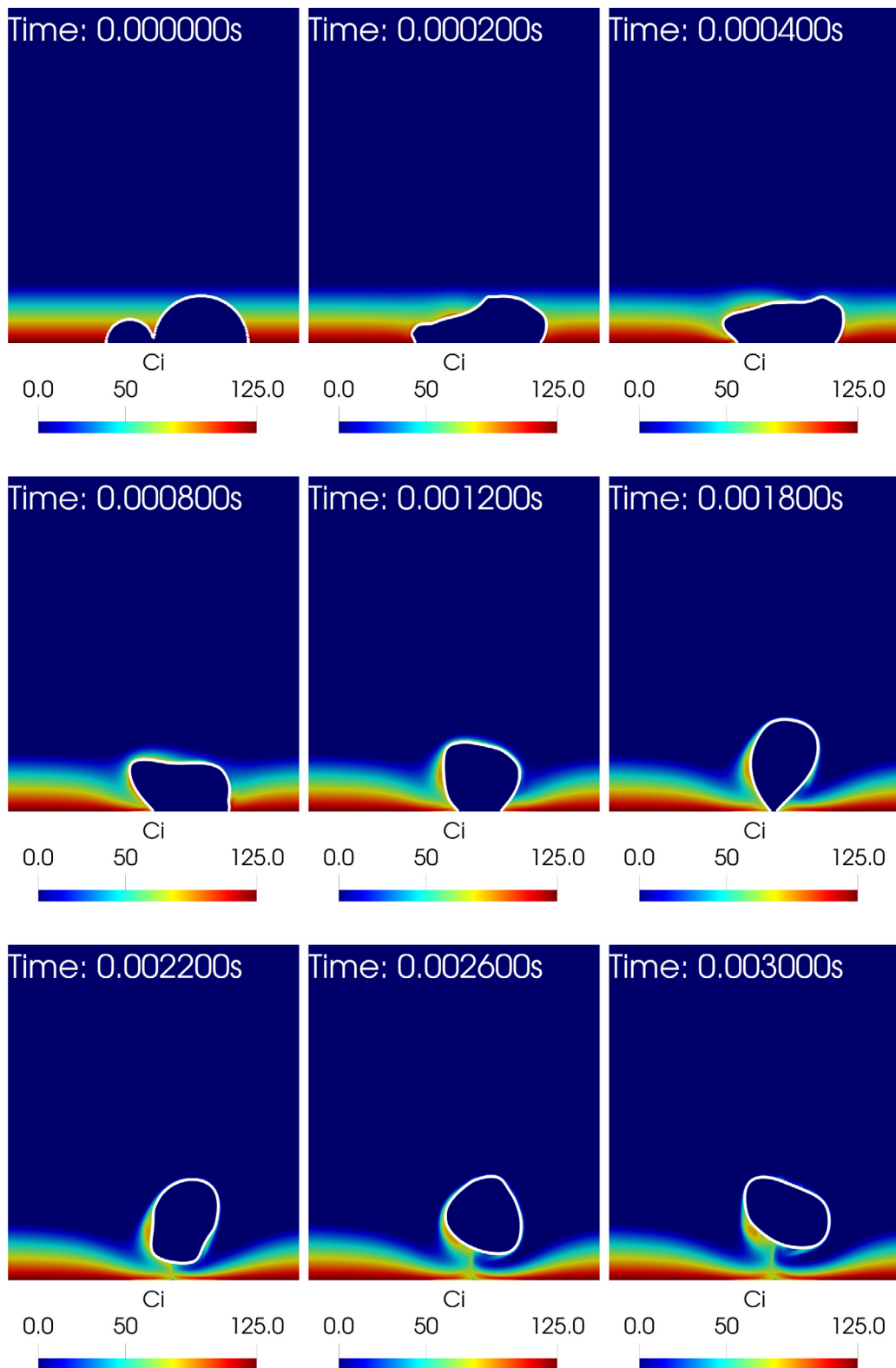
Fig. 19. The evolution of the interface and the concentration of the dissolved gas (mol/m^3) as the bubble coalescence and evolves in the case of DC1 (with initialized bubbles of radii equal to 400 micrometers). Note the necking process (between 0s-0.4ms), propagation of deformation waves along the bubble interface which leads to the lifting of the bubble (between 0.6ms-2ms) and detachment as well as the oscillations of the bubble surface leading to elongation and flattening (2ms-4ms). The white line represents the interface which is plotted at $\alpha_1 = 0.5$. See supplementary materials for more information.

Fig. 20. The evolution of the interface and the concentration of the dissolved gas (mol/m^3) as the bubble coalescence and evolves in the case of DC2 (with initialized bubbles of radii equal to 200 micrometers and 400 micrometers). Note the necking process (between 0s-0.2ms), propagation of deformation waves along the bubble interface which leads to the lifting of the bubble (between 0.4ms-1.2ms) and detachment as well as the oscillations of the bubble surface leading to elongation and flattening (1.8ms-3ms). The white line represents the interface which is plotted at $\alpha_1 = 0.5$. See supplementary materials for more information.
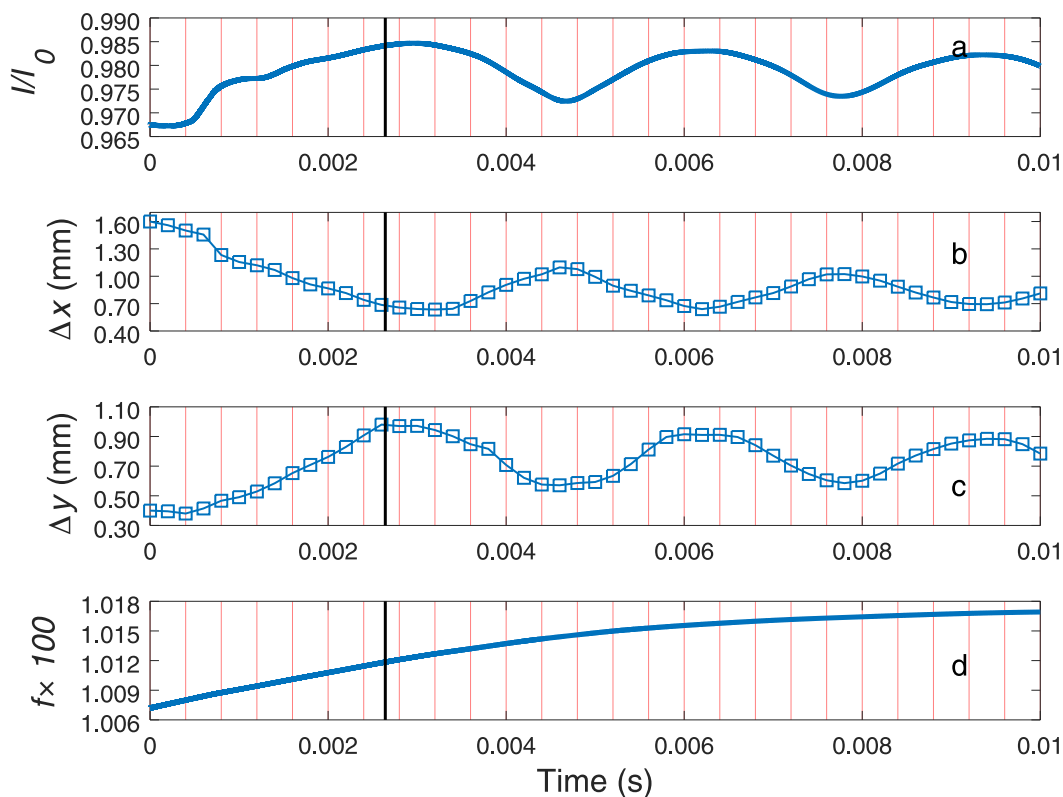
Fig. 21. The temporal variation of various relevant parameters as two equally sized bubbles coalescence and detachment in DC1: a) normalized current (I/I_0), b) horizontal deformation (Δx), c) vertical deformation (Δy), d) normalized volume of bubble (f). The vertical black line indicates the detachment time, τ_d, and the vertical red lines are equidistant grid line at every 0.0004s to enable comparison between the plots.

TC1c, results in a larger fraction of the electrode covered by the bubble and Δx, which results in reduction of current when compared to TC1a. As the bubble which has detached, TC2a-h, has the same volume as the bubble present on electrode, both TC1a and TC1c, the detachment is observed to result in increase in the current as observed in experimental works like [70].

5. Results and discussion

5.1. Single bubble evolution

Effect of contact angle. The contact angle is an important parameter which has been experimentally observed to effect the bubble detachment [5]. Larger the value of contact angle (θ), measured in the liquid, less hydrophilic the electrode surface becomes which leads to difficulty in the bubble detachment. The wetting condition at the electrode is investigated with three cases: SCT0, SCT1, and SCT2 which differ by the contact angle (θ) defined at the electrode which is equal to 15°, 30° and 45° respectively.

As shown in Fig. 9, the bubble detaches in the cases of SCT0 and SCT1 whereas it remains adhered to the electrode for the case of SCT2. As the initialized bubbles for all three cases are of radius equal to 400 micrometers, gravitational force can be ruled out as the reason for the observed detachment. The detachment, observed in the simulation, is a result of the momentum induced as a result of deformation wave travelling at the interface due to the difference between the contact angle of the initialized bubble and the equilibrium contact angle at the electrode. As all three simulations start with the same initial bubble of radius equal to 400 micrometers and a contact angle of 90°, the momentum induced for SCT0 would be larger compared to the other two cases (as a result of larger deviation between the initial and equilibrium conditions). In the cases of SCT0 and SCT1, the bubble is able to detach as the initial momentum causes a 'lift' which overcomes adhesion due to surface tension. The initial momentum in SCT2 causes the bubble to deform and lift, until around 0.0016 s (see Fig. 10), but the bubble does not detach and subsequently surface tension pulls the bubble down in an attempt to reach the equilibrium shape based on the wetting condition. This dynamic process continues until the bubble reaches an equilibrium shape which is dictated by the surface tension and gravitational force which is observed in damping of $1 - \Theta$ with time, observed in Fig. 10. Although bubble detachment is observed for both SCT0 and STC1, the initial momentum imparted to the bubble is larger for the former which results in a smaller τ_d, see Table 6.

Table 6
The variation of detachment time (τ_d) of the bubble from the electrode surface for various contact angles.

	SCT0 ($\theta = 15°$)	SCT1 ($\theta = 30°$)	SCT2 ($\theta = 45°$)
τ_d	0.00138 s	0.00169 s	No detachment

Table 7
Comparison of the time averaged bubble deformations and current obtained for SCT0 and SCT1.

Case	$\overline{\Delta x}$ (mm)	$\overline{\Delta y}$ (mm)	$\bar{I}/I_0$
SCT0	0.586	0.537	0.98996
SCT1	0.572	0.553	0.99046

For the case of SCT0, the detachment of the bubble results in its deformation and growth as it rises up through the concentration boundary layer, as shown in Fig. 9. This deformation and growth results in temporal variations of current, see Fig. 11. Before the bubble detaches, the bubble gets lifted and vertically elongated due to the initially imparted momentum, see Fig. 9, this results in increasing Δy and decreasing Δx. The increase in current before detachment is a direct consequence of the reduction of the electrode region covered by the bubble (indicated by $1 - \Theta$) which reduces from the initial bubble diameter of 0.8mm to nearly half at detachment, see Fig. 11c. As a result of the bubble leaving the surface, the current increases from $t = 0$s to the detachment. Once the bubble detaches, the bubble shape oscillates i.e. it first gets flattened (larger Δx) and then gets elongated (larger Δy), see Fig. 11b-c. These oscillations progressively gets damped as the bubble rises up. As the bubble gets flattened, the projection of the bubble on the electrode becomes larger which yields lower current in contrast to vertical elongation when projection is reduced and current increases, see Fig. 11b-c. The existence of surface oscillations as bubbles rise were also experimentally reported in detached bubble (in the order of few hundred micrometers) in the work by [71]. Similar trends, in the variation between bubble deformations and current, is also visible for the bubble evolving in SCT1 (see Fig. 12). Instead of the single peak in I/I_0 near detachment observed for SCT0, SCT1 produces an additional peak around 0.002s which is a consequence of the detached bubble staying close to the electrode for longer than SCT0 due to the smaller rise velocity, see Fig. 15. The rise velocities of SCT0 and SCT1, see Fig. 15, show substantial differences after detachment and this can be explained as a result of the bubble in SCT1 rises up mostly due to buoyancy where as in SCT0 the momentum 'left-over' after detachment also aids in the evolution. Apart from the variation of current due to bubble detachment and deformation, as the bubble rises, the current also reduces with the vertical distance from the electrode, which agrees with the observations in Table 5. Although both SCT0 and SCT1 produce larger current at detachment, when compared to the current at $t = 0$ s, the current reduces as a result of increase in the Δx and f once the bubble has detached, as well as the reduction in current observed in vertical distance.

Due to the quick ascent of the bubble in SCT0, through the concentration boundary layer, the increase in the volume of the bubble is larger for SCT1 when compared to SCT0, see Fig. 11d and Fig. 12d. Although the growth of the bubble occurs when the it is within the concentration boundary layer, its effect on current is visible only when bubble surface oscillations have damped, see Fig. F.28a-b. Due to the larger rise velocity in SCT0 compared to SCT1, the drag force acting on the rising bubble in the former is larger which results in a bigger Δx and consequently a smaller current, see Table 7. As the bubble detaches from the electrode surface, the convection established seems to drag the dissolved hydrogen in the concentration boundary layer in the wake of the rising bubble as observed in Fig. 13 and Fig. 14.

In the case of SCT2, the initially imparted momentum causes the bubble to deform and reach an equilibrium shape which influences the current. In this attempt to reach equilibrium shape, $1 - \Theta$ increases and the effective radius of the bubble shielding the electrode (indicated by Δx) effectively reduces causing current to increase, see Fig. 16a-b. The change in the bubble size is reflected in the transition of Δx from to 0.8mm initially to a more elongated bubble towards the end of the simulation, reducing Δx. As the bubble remains within the concentration boundary layer, in this case, its growth is larger compared to SCT0 and SCT1 cases. Inspite of the larger growth rate in SCT2, the effect on current is visible only towards the latter part of the simulation when the bubble deformations has damped, see Fig. F.28c. It should be noted that in the case of STC2, as the bubble remains on the electrode, the convection in this case is different from SCT0 and SCT1 which is reflected in the concentration distribution of the dissolved gases, see Fig. 17.

Effect of the initial concentration boundary layer thickness. In order to study the influence of the concentration boundary layer thickness, set as $\delta = 0.5$mm in the previous simulations, three different cases which differ only by the values of δ is used: SCT1 ($\delta = 0.5$mm), SCT1BL- ($\delta = 0.3$mm) and SCT1BL+ ($\delta = 0.8$mm). The contact angle at the electrode as well as other computational setting are set based on SCT1. The initialized distribution of the dissolved gas concentration used in these three simulations is based on Eq. 22.

As the bubble travels through the concentration boundary layer, it grows due to interfacial mass transfer driven by local supersaturation. As larger concentration boundary layer thickness represents a greater region which is supersaturated, the largest growth is observed in SCT1BL+ (equal to 0.8mm) followed by SCT1 (equal to 0.5mm) and SCT1BL- (equal to 0.3mm)

Table 8
The initialized bubbles used in the coalescence simulations.

Case	Bubble 1		Bubble 2			
	x_c (mm)	y_c (mm)	x_c (mm)	y_c (mm)	f	$1 - \Theta$
DC1	0.0046	0.0000	0.0054	0.0000	0.0101	0.84
DC2	0.0048	0.0000	0.0054	0.0000	0.0063	0.88

with an increase in bubble volume of around 4%, 1.5% and 0.5% of the initial bubble volume. The effect of the increase in the bubble volume on current is only visible when the bubble deformations has damped, see Fig. 18a. Despite the increase in bubble volume, its effect on rise velocity of the bubble and detachment time is mostly negligible, see Fig. 18.

5.2. Coalescence driven bubble evolution

As observed in the static bubble simulations, the presence of two bubbles on the electrode which produces a single detached bubble provides a larger increase in current when compared to a single bubble of equivalent volume detaching, see Table 5. In order to investigate the dynamic effect of the coalescence of continuum scale hydrogen bubbles, two cases, DC1 and DC2, in which bubbles are initialized based on Table 8 such that the x_c of the bubbles are offset by the radius from $x = 5$mm. The boundary conditions are set analogous to single bubble evolution from the electrode with $\theta = 45°$, i.e. SCT2.

Contrary to the single bubble in SCT2 which remained adhered to the surface, both DC1 and DC2, under identical wetting conditions at the electrode, show detachment of the coalesced bubble, see Fig. 19 and Fig. 20. Although the difference between the initialized contact angle of the bubble and the equilibrium wetting condition at the electrode provides some initial momentum, like the case of SCT2, the coalescence process of the bubbles is the driver of the bubble detachment. During coalescence, the surface tension acts to minimize the surface area of the bubbles, which results in dynamic changes in the interface which can be categorized into neck formation between the bubbles, deformation wave propagation at the interface which results in the lifting of the bubble, detachment of the bubble and the oscillations in bubble shape, see Fig. 19 and Fig. 20. These stages during coalescence has also been observed during the in the experimental work by [71], using two equally sized bubbles of radii equal to 0.4 mm. The deformation waves, which are qualitatively analogous to the ones observed in the second stage of the bubble coalescence in DC1 and DC2 in Fig. 19 and Fig. 20, are reported to be capillary waves in the work by [71]. In DC1, as these deformation waves are symmetric about $x = 5$mm, see Fig. 19, the detached bubble is also symmetric about the same axis. On the other hand, the asymmetric propagation of the deformation wave towards the smaller bubble in DC2, see Fig. 20, results in translation of the detached bubble along the electrode. Interestingly the deformation induced during coalescence in DC2 results in a quicker detachment of the final bubble compared to DC1 in spite of the larger bubble volume in the latter, see Fig. 21 and Fig. 22. The detachment of bubble in the DC1 and DC2 yields larger current when compared to when the two bubbles where present on the electrode, see Fig. 21a and Fig. 22a. Before detachment, as surface tension attempts to reduce the surface area of the bubble via coalescence, Δx reduces until detachment as shown in Fig. 19 and Fig. 20. The deformation of the detached bubble also has a substantial impact on the current obtained i.e. larger projection of the bubble on the electrode, indicated by larger Δx, results in lower current. It should also be pointed out that, during the coalescence driven bubble evolution in DC1 and DC2 the bubble grew by around 0.97% and 1.34% when compared to the initial bubble volume respectively. The difference in the growth rate between the two cases is a result of larger amount of dissolved gas which is present near the detached bubble in DC2, see Fig. 19 and Fig. 20, due the convection established during the coalescence and detachment.

6. Conclusions

In this paper, a new Volume of Fluid (VOF) based framework to study the continuum scale evolution of hydrogen bubble in an electrochemical system is presented. The proposed framework is based on the VOF framework available in Open-FOAM® 6, which uses an algebraic VOF method to capture the interface. The transport of the dissolved gas is based on the Compressive Continuous Species Transport model [29], the driving force for interfacial mass transfer is based on the phenomenological Fick's 1st law and relevant source terms are computed based on [27], charge conservation is ensured using Gauss's law and Ohm's law [39] and surface tension model as described by [25,26]. The proposed solver is verified by comparison to the analytical solution for 2D bubble growth in a uniformly supersaturated unbounded medium by [68,69], 2D stationary bubble (which has an analytical solution) and 2D rising bubbles (based on the computational benchmark proposed by [66]). Additionally the variation of the current predicted by the solver is compared qualitatively to reported observations in experiments like [70].

The single bubble simulations showed that the observed detachment of the bubble is a result of the deviation between the contact angle of the initialized bubble and the wetting condition at the horizontal electrode. In order to accurately simulate the process, hybrid VOF methods like [39,40,43] are required to generate larger bubbles which are consistent with the eleectrode wetting conditions. Regardless, single bubble simulations showed quicker bubble detachment with smaller contact angles as a result of the stronger hydrophilic nature of the surface. When the bubble is present on the surface, the
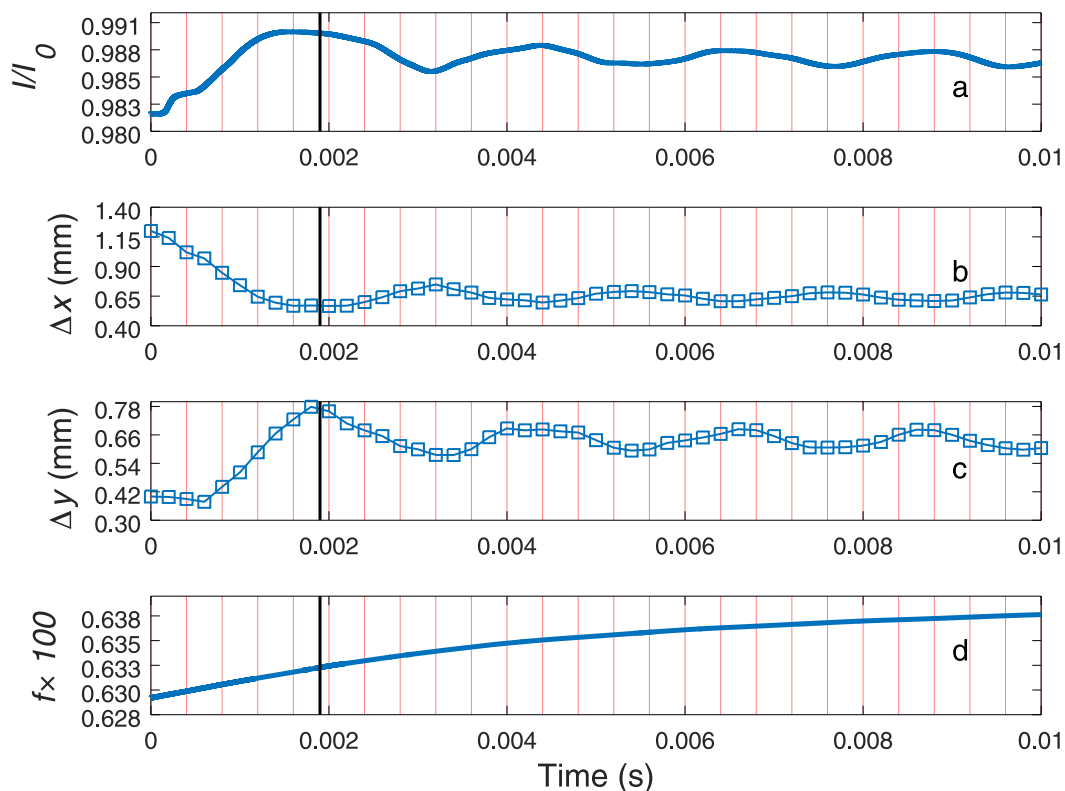
Fig. 22. The temporal variation of various relevant parameters as two unequally sized bubbles coalescence and detachment in DC2: a) normalized current (I/I_0), b) horizontal deformation (Δx), c) vertical deformation (Δy), d) normalized volume of bubble (f). The vertical black line indicates the detachment time, τ_d, and the vertical red lines are equidistant grid line at every 0.0004s to enable comparison between the plots.

reduction in the area of the bubble covering the electrode is observe to influence the current. At detachment, the current obtained is larger than at the initial state of the system. Once the bubble has detached, the surface of the bubble is observed to show oscillations which causes the bubble to flatten and elongate analogous to the experimental observations by [71]. These deformation of the bubble cause the variation in the current i.e. larger horizontal deformation (Δx), which means larger projected area of the bubble, results in lower current due to the larger distortion of the current path lines. These distortions in the current pathlines are observed for several bubble radius as shown previously by [38]. Interestingly, the current is observed to decrease as it rises up, after the detachment. This can be explained as the result of the reduction of the effective resistance by lowering the characteristic length experienced by the current lines when the detached bubble is closer to the electrode, see Fig. 8. As the bubble rises up, the bubble shape is dictated by the surface tension and drag forces which means that a bubble with higher rise velocity tends to be flatter or has a larger Δx which produces less current, see Table 7. As the bubble evolves, in the cases it detaches, the convection established by the rising bubble also drags some dissolved gas up with it, see Fig. 13 and Fig. 14. Although the bubble drags the dissolved gas as it rises up, the bubble grows predominately within the concentration boundary layer. The effect of the bubble growth is not visible in detachment time and rise velocity but it has a noticeable effect on current evolution only when the bubble surface oscillations have damped, see Fig. 18 and Fig. F.28.

The coalescence driven bubble detachment shows an increase in current as bubble detaches and rises up, see Fig. 21 and Fig. 22, when compared to a single bubble simulations, see Fig. 11 and Fig. 12. This larger increase in current in coalesce driven detachment is a result of value of higher value of $1 - \Theta$ at $t = 0$s when compared to single bubble simulations. In the coalescence driven case, the current is also observed to vary with the bubble deformation, see Fig. 21 and Fig. 22. Simulations considering the coalesce of two bubbles show three distinct regimes: necking, propagation of the deformation waves, and detachment of the bubble, which has also been reported in the work by [71]. The simulations also shows the existence of travelling deformation waves at the interface, observed by [71]. The propagation of these deformation waves is found to influence the detachment process, as observed in the quicker detachment of the DC2 which has a smaller bubble compared to DC1, as well as cause the translation of the detached bubble along the electrode. The simulations suggests that the bubble detachment, at least for continuum scale bubbles, are primarily driven by coalescence rather than bubble growth by interfacial mass transfer.

Disclosure of conflicts of interest

The authors declare that they have no known competing financial interests or personal relationships that could have appeared to influence the work reported in this paper.

Acknowledgement

Appendix A. Modelling surface tension using Sharp Surface Force approach

The surface tension term ($\vec{F}_{ST}$) in the momentum equation is typically calculated using Continuum Surface Force (CSF) model, proposed by [72], as equal to $\sigma \kappa \nabla \alpha_1$ where σ is surface tension and κ is the interface curvature which is calculated as $\kappa = -\nabla \cdot \vec{n}$. As α_1 is a discontinuous, see [21], the calculation of κ is prone to numerical errors which generates spurious velocities, see [21,24,25,30,31]. These spurious velocities alter interfacial mass transfer [27,73] and may cause random walk of bubbles [59,26]. A relatively easy way to address these numerical artifacts is by using Sharp Surface Force (SSF) model, which was proposed by [54] and then used to simulate surface tension driven flows in works like [25,26,74]. The surface tension term is computed using the Sharp Surface Force (SSF) model, as described in [25,26], as

$$\vec{F}_{ST} = \sigma \kappa_{final} \nabla \alpha_{sh},$$

where κ_{final} is the interface curvature and α_{sh} is the sharpened volume fraction of phase 1 which is determined based on Eq. 11. The interface curvature (κ_{final}), used by the Sharp Surface Force (SSF) model, is calculated based the following steps [25,26]:

1. Three step smoothening operation of α_1 (which is stored at cell centers), i.e. $i=1,2,3$, by interpolating it from cell center to face center and back which can be represented as

$$\alpha_{i+1}^s = C \Big\langle < \alpha_i^s >_{c \to f} \Big\rangle_{f \to c} + \Big(1 - C\Big) \alpha_i^s, \tag{A.1}$$

   where $C = 0.5$, $< \alpha_1 >_{c \to f}$ interpolates α_1 from cell center to face and $\alpha_1^s = \alpha_1$.

2. Interface normal is then calculated as $\vec{n} = \nabla \alpha_4^s / (|\nabla \alpha_4^s| + \delta)$ where $\delta = 10^{-8} / \left(\frac{\sum_N V_i}{N} \right)^{1/3}$ is used to prevent denominator of $\vec{n}$ from becoming zero. Once interface normal is calculated, it is corrected for contact angle specified at the wall by $\vec{n}|_w = \vec{n}_w \cos\theta + \vec{t}_w \sin\theta$ where θ is the contact angle defined at the wall, $\vec{n}|_w$ is the interface normal at the wall, $\vec{t}_w$ and $\vec{n}_w$ are the tangent and normal vectors to the wall [25,54,75].

3. Based on the interface normal, the initial estimate of the interfacial curvature (κ_1) is calculated as $\kappa_1 = -\nabla \cdot \vec{n}$.

4. Two step smoothening of the interface curvature ($i = 1,2$) in the direction normal to the interface described as

$$\kappa_{i+1}^s = 2\sqrt{A}\kappa_1 + (1 - 2\sqrt{A}) \frac{\Big\langle < w\kappa_i^s >_{c \to f} \Big\rangle_{f \to c}}{\Big\langle < w >_{c \to f} \Big\rangle_{f \to c}}, \tag{A.2}$$

   where $A = \alpha_c(1 - \alpha_c)$, α_c is defined as $\min(1, \max(\alpha_1, 0))$, $\kappa_1^s = \kappa_1$ and $w = \sqrt{A + 0.001}$.

5. Calculate the interface curvature using a weighted interpolation method as

$$\kappa_{final} = \frac{< w\kappa_3^s >_{c \to f}}{< w >_{c \to f}}. \tag{A.3}$$

Appendix B. Imbalance in liquid/bubble and dissolved gas

As the proposed framework treats the growth and evolution of a bubble, based on Eq. 17, the volume of liquid should in principle remain constant in the simulation. Fig. B.23 shows the imbalance in the liquid/bubble during the simulation to be much lower than 0.1%. The imbalance in the amount of dissolved gas is due to the presence of dissolved gas in the bubble, this is lower than 0.1% of the dissolved gas in the computational domain (which is around 2.9×10^{-10} mol despite the addition of dissolved gas via electrochemical reactions), see Fig. B.24.
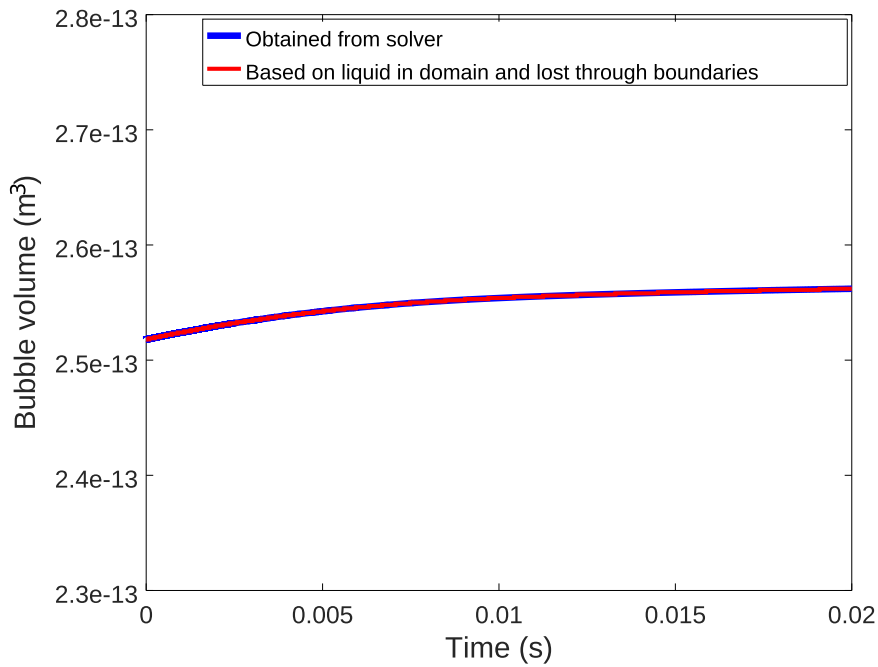
Fig. B.23. Temporal variation of the mass imbalance in the system indicated as the bubble volume obtained from the solver (equal to $\int \alpha_2 dV$) and the difference in the total volume of the domain and the volume of liquid present in the domain which is adjusted for the liquid lost through the boundaries.
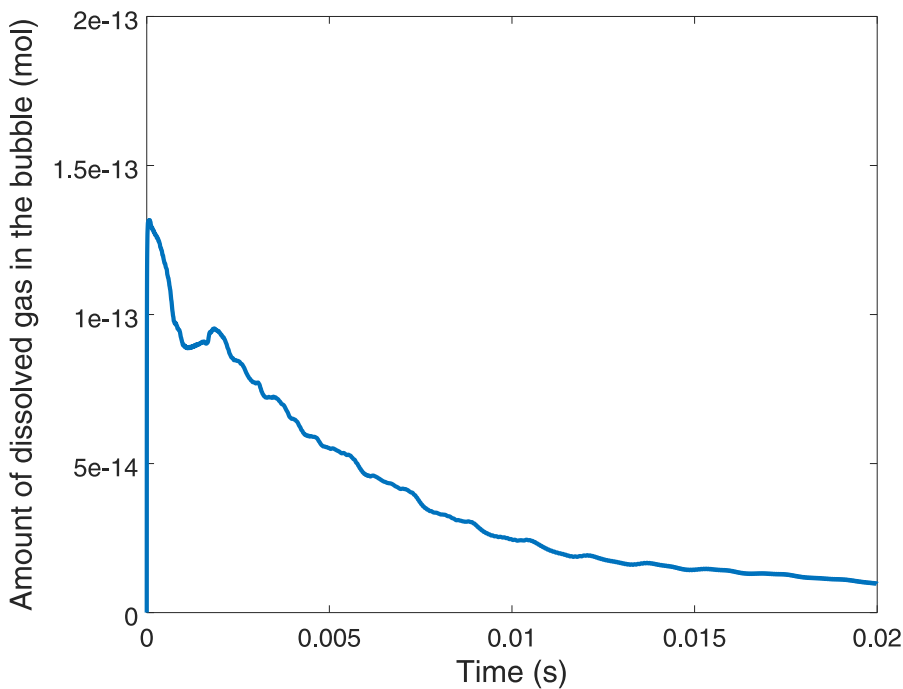

Fig. B.24. Temporal variation of the amount of dissolved gas in the bubble which is calculated as $\int C_i \alpha_2 dV$.

Appendix C. Mesh convergence

As the proposed framework, which is based on the Finite Volume Method, relies on the mesh to descritize the governing equations, it is important to ensure that the solution is not independent of these errors. In order to study the mesh convergence of the solution, for the case of SCT1, is studied using six different meshes: 400×200, 564×282, 800×400, 1128×564, 1600×800 and 2256×1128 which represents 32, 45, 64, 90, 128 and 180 cells across the diameter of the ini-
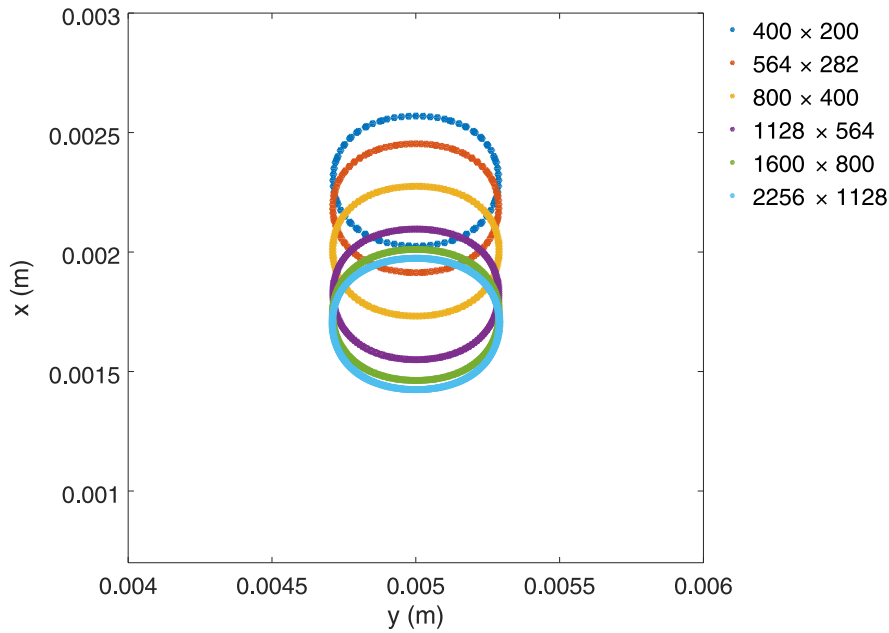
Fig. C.25. The interface of the bubble at 0.02s for SCT1 for the six meshes considered in the convergence study..

tialized bubble respectively. The grid convergence is studied by comparing the bubble shape ($\alpha_1 = 0.5$) at 0.02s in Fig. C.25. As the variation between the bubble shapes for the finest two meshes are negligible, 1600 × 800 is used in the simulations considered in the paper. Additionally, the difference in the current obtained between the two finest meshes, 1600 × 800 and 2256 × 1128, at 0.02s is less than 0.01%.

Appendix D. Temporal convergence

As surface tension is dominant in the electrochemical bubble evolution phenomena, its modelling can be influenced by the well known problem of spurious velocities in VOF based methods [21,24,25]. These spurious velocities which are numerical artifacts can result in non-physical flow velocities/deformations of the interface can reduce the accuracy of the simulation as observed in [26,27,73]. These spurious velocities are generated in the proposed solver due to inaccuracies in the curvature calculation used in surface tension modelling, see [26]. As the surface tension is treated explicitly in the proposed solver, the spurious current in the simulation can increase over time if an appropriate time step is not used which would lead to a dependence of the solution on time step [21,25]. The most commonly used time step constraint which is used to prevent the growth of these spurious velocities, is the one proposed by [72]:

$$\Delta t < \sqrt{\frac{\rho_{avg}\Delta_x^3}{2\pi\sigma}}, \tag{D.1}$$

where Δ_x is the mesh cell size and ρ_{avg} is the average density between the two phases. In order to ensure the simulations discussed in the paper are not influenced by spurious velocities, the predictions of the proposed solver for SCT1 and SCT2 cases (due to the lower rise velocity when compared to SCT0) are compared with maximum time step based on Courant number of 0.05 and Eq. D.1, which is equal to 5.25×10^{-7}s.

Comparison of I/I_0, rise velocity, normalized bubble volume and bubble coverage for SCT1 and SCT2, see Fig. D.26 and Fig. D.27, shows that the time step resolution does not result in much change to these parameters for the duration of the simulation. This can be explained by understanding the velocity field induced by the motion of the interface to be much larger than the nonphysical velocity field generated by the spurious velocities. As a result, in the case of SCT1, the time step constraint can be ignored to obtain reasonable results and to save the computational overhead imposed Eq. D.1. For the case
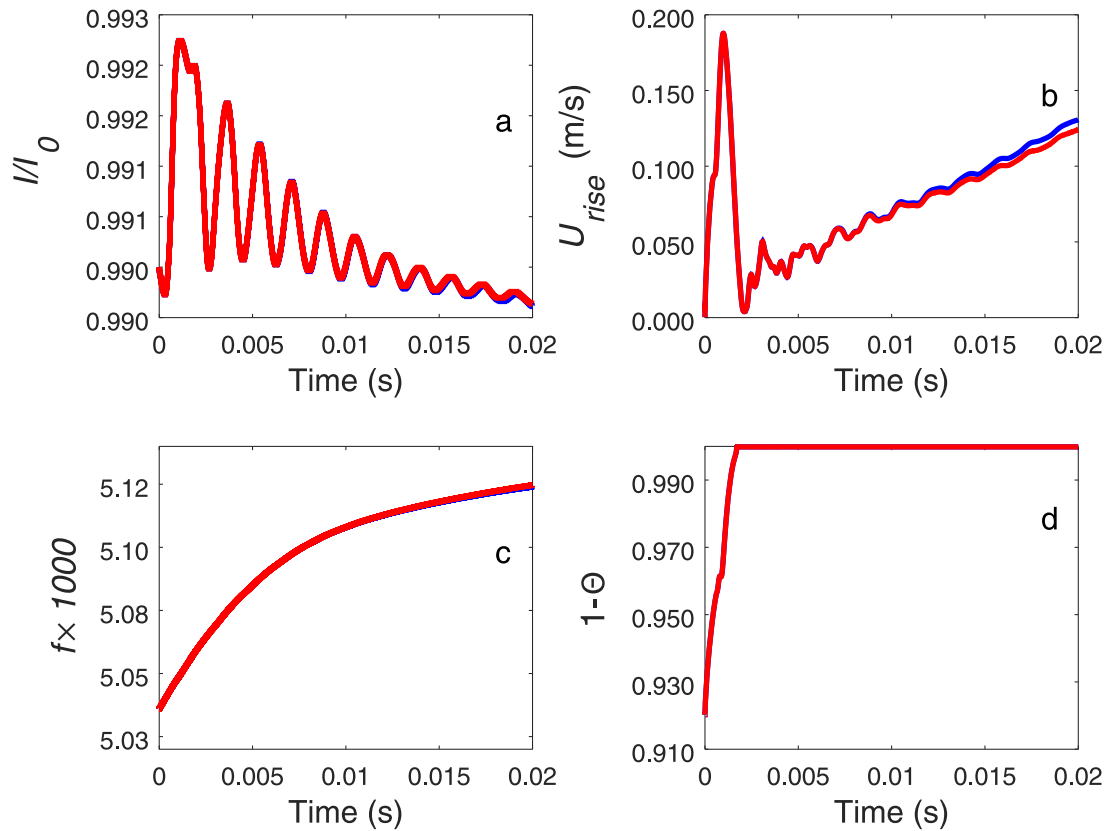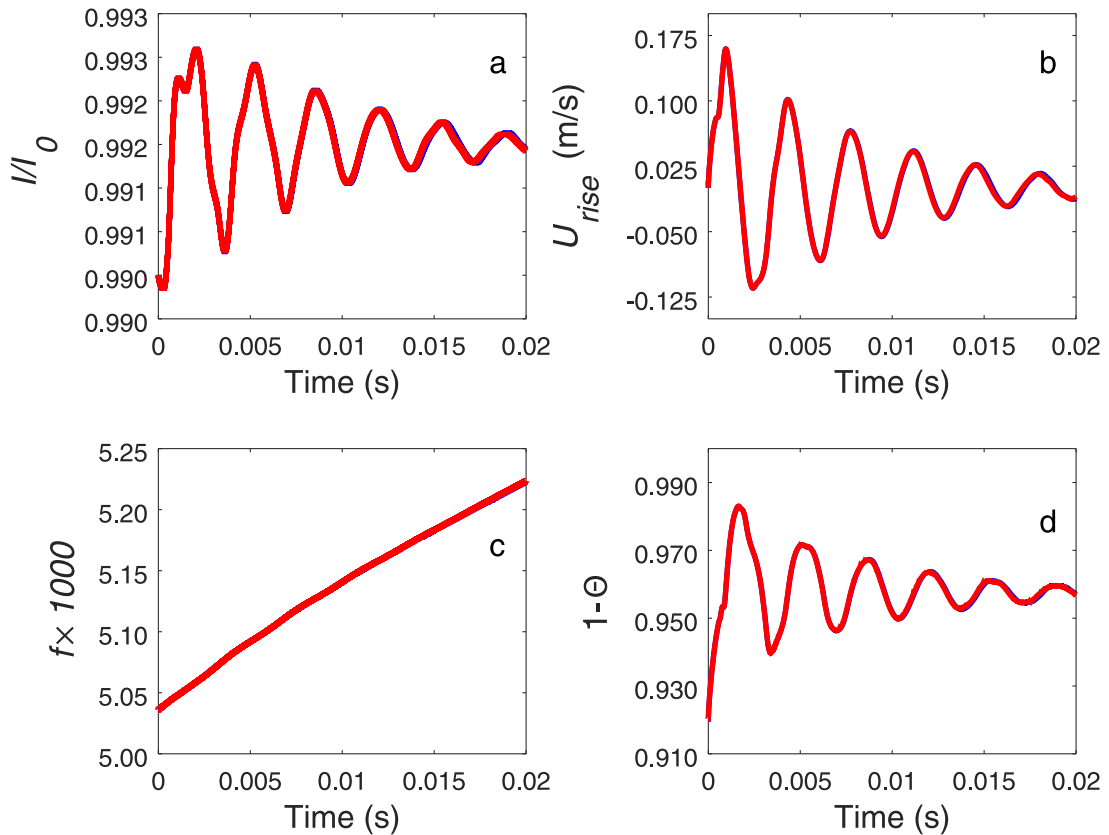
Fig. D.26. Comparison of a) I/I_0, b) rise velocity and c) normalized bubble volume (f), d) $1 - \Theta$ obtained for bubble evolution for SCT1 (contact angle at the electrode set at 30°) for simulations based on time step based on Courant number (———) and Brackbill time step constraint (———).

of SCT2, it should be pointed out that in order to simulate the bubble reaching equilibrium shape on the electrode, when physically the velocity in the domain should reduce to zero, it would be necessary to suppress spurious velocities by using more advanced surface tension modelling approaches (most probably based on the geometric VOF [22]) and impose time step constraint to prevent the growth of these numerical artifacts.

Appendix E. Estimation of the initial concentration boundary layer thickness

The thickness of hydrodynamic boundary layer, for a laminar flow over a flat plate, according to [76], is equal to

$$\delta_H = 5\sqrt{\frac{\nu_1 x}{U_\infty}}. \tag{E.1}$$

where x is the distance from the leading edge of the plate and U_∞ is the free stream flow velocity. The concentration boundary layer thickness (δ_C) can be expressed in terms of δ_H as

$$\frac{\delta_C}{\delta_H} = \left(\frac{\nu_1}{D_{i,1}}\right)^{-1/3} = Sc^{-1/3}, \tag{E.2}$$

where Sc is the non-dimensional Schmidt number. The above equation can be rearranged to get an expression of the concentration boundary layer thickness as

$$\begin{aligned}\delta_C &= \left(\frac{\nu_1}{D_{i,1}}\right)^{-1/3} 5\sqrt{\frac{\nu_1 x}{U_\infty}} \\ &= 5\nu_1^{1/6} D_{i,1}^{1/3} x^{1/2} U_\infty^{-1/2}.\end{aligned} \tag{E.3}$$

Eq. E.3 can be averaged over the length of the flat plate (L) to get an average concentration boundary layer equal to

$$\overline{\delta_C} = \frac{1}{L}\int_0^L 5\nu_1^{1/6} D_{i,1}^{1/3} x^{1/2} U_\infty^{-1/2} dx \tag{E.4}$$

$$\overline{\delta_C} = \frac{10}{3}\nu_1^{1/6} D_{i,1}^{1/3} U_\infty^{-1/2} L^{1/2} \tag{E.5}$$

Fig. D.27. Comparison of a) I/I_0, b) rise velocity and c) normalized bubble volume (f), d) $1 - \Theta$ obtained for bubble evolution for SCT2 (contact angle at the electrode set at 45°) for simulations based on time step based on Courant number (──) and Brackbill time step constraint (──).

For electrode length scale (L) equivalent to 10^{-2}m, $\nu_1 = 9.89 \times 10^{-7}$ m²/s, $D_{i,1} = 4.8 \times 10^{-9}$ m²/s and U_∞ in the order of 0.1m/s gives $\bar{\delta}_C$ in the order of 10^{-4}m. In order to simplify notation in the main body of the paper, $\bar{\delta}_C$ is written as δ.

Appendix F. Comparison of current obtained with and without mass transfer driven bubble growth

In order to compare the effect of bubble growth on the current obtained, the cases without any mass transfer is simulated by using analogous setups to SCT0, SCT1 and SCT2 for the initial and boundary conditions except for the electrochemical reactions which was replaced with a zero gradient condition at the wall in addition to not initilizing a concentration boundary layer. This prevent the growth of the bubble due to interfacial mass transfer driven by supersaturation. The comparison of the current obtained in SCT0, SCT1 and SCT2 with and without bubble growth is plotted in Fig. F.28.
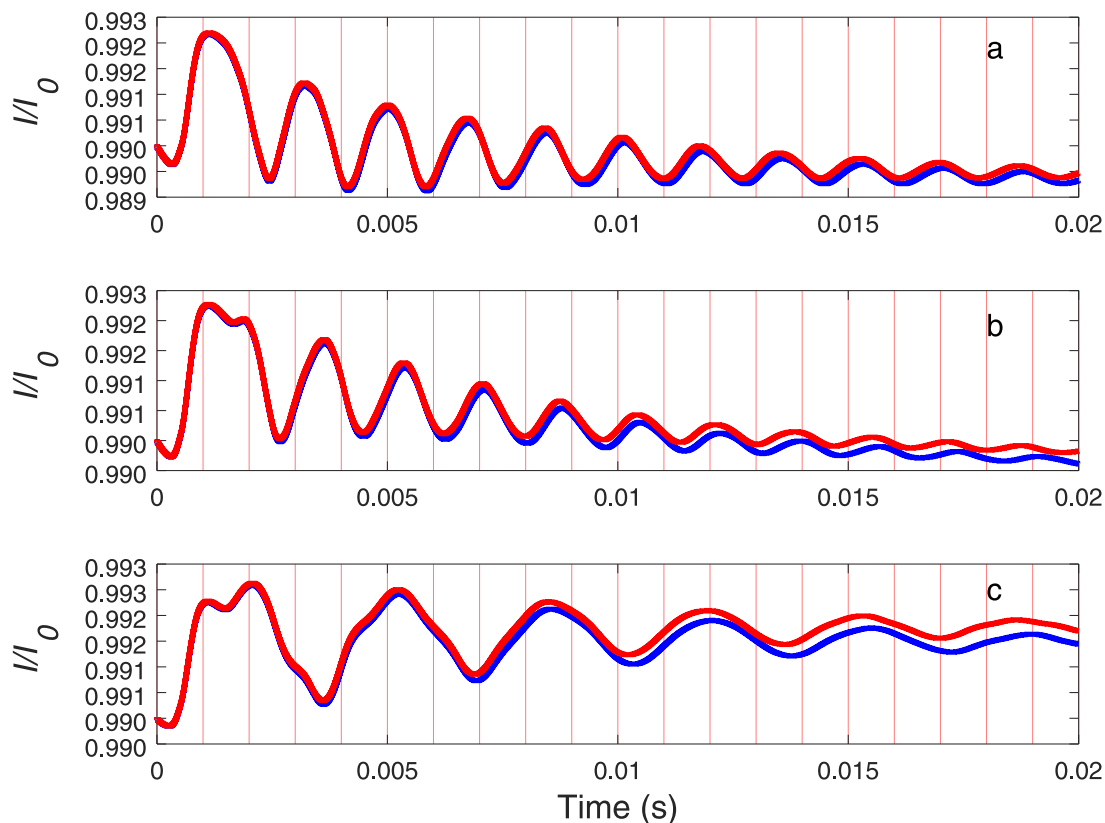
Fig. F.28. Comparison of the normalized current (I/I_0) for various contact angles with (▬) and without (▬) interfacial mass transfer driven bubble growth: a) SCT0, b) SCT1 and c) SCT2. The vertical red lines are equidistant grid line at every 0.001s to enable comparison between the plots.

Supplementary material

Supplementary material associated with this article can be found, in the online version, at doi:10.1016/j.apm.2021.05.007.

References

[1] K. Scott, Chapter 1 Introduction to electrolysis, electrolysers and hydrogen production, in: Electrochemical Methods for Hydrogen Production, The Royal Society of Chemistry, 2020, pp. 1–27, doi:10.1039/9781788016049-00001.
[2] M.A. Khan, H. Zhao, W. Zou, Z. Chen, W. Cao, J. Fang, J. Xu, L. Zhang, J. Zhang, Recent progresses in electrocatalysts for water electrolysis, Electrochemical Energy Reviews 1 (4) (2018) 483–530, doi:10.1007/s41918-018-0014-z.
[3] H. Jin, J. Joo, N.K. Chaudhari, S.-I. Choi, K. Lee, Recent progress in bifunctional electrocatalysts for overall water splitting under acidic conditions, ChemElectroChem 6 (13) (2019) 3244–3253, doi:10.1002/celc.201900507.
[4] Z. Lei, T. Wang, B. Zhao, W. Cai, Y. Liu, S. Jiao, Q. Li, R. Cao, M. Liu, Recent progress in electrocatalysts for acidic water oxidation, Adv Energy Mater 10 (23) (2020) 2000478, doi:10.1002/aenm.202000478.
[5] G.B. Darband, M. Aliofkhazraei, S. Shanmugam, Recent advances in methods and technologies for enhancing bubble detachment during electrochemical water splitting, Renewable Sustainable Energy Rev. 114 (2019) 109300, doi:10.1016/j.rser.2019.109300.
[6] X. Zhao, H. Ren, L. Luo, Gas bubbles in electrochemical gas evolution reactions, Langmuir 35 (16) (2019) 5392–5408, doi:10.1021/acs.langmuir.9b00119.
[7] C. Brussieux, P. Viers, H. Roustan, M. Rakib, Controlled electrochemical gas bubble release from electrodes entirely and partially covered with hydrophobic materials, Electrochim. Acta 56 (20) (2011) 7194–7201, doi:10.1016/j.electacta.2011.04.104.
[8] D. Fernández, P. Maurer, M. Martine, J.M.D. Coey, M.E. Möbius, Bubble formation at a gas-evolving microelectrode, Langmuir 30 (43) (2014) 13065–13074, doi:10.1021/la500234r.
[9] X. Yang, D. Baczyzmalski, C. Cierpka, G. Mutschke, K. Eckert, Marangoni convection at electrogenerated hydrogen bubbles, Phys. Chem. Chem. Phys. 20 (2018) 11542–11548, doi:10.1039/C8CP01050A.
[10] A. Bashkatov, S.S. Hossain, X. Yang, G. Mutschke, K. Eckert, Oscillating hydrogen bubbles at pt microelectrodes, Phys. Rev. Lett. 123 (2019) 214503, doi:10.1103/PhysRevLett.123.214503.
[11] A. Taqieddin, M.R. Allshouse, A.N. Alshawabkeh, Editors' choice- critical review—mathematical formulations of electrochemically gas-evolving systems, J. Electrochem. Soc. 165 (13) (2018) E694–E711, doi:10.1149/2.0791813jes.
[12] K.J. Vachaparambil, K.E. Einarsrud, Explanation of bubble nucleation mechanisms: a gradient theory approach, J. Electrochem. Soc. 165 (10) (2018) E504–E512, doi:10.1149/2.1031810jes.
[13] F. Hofbauer, I. Frank, Electrolysis of water in the diffusion layer: first-principles molecular dynamics simulation, Chemistry A European Journal 18 (1) (2012) 277–282, doi:10.1002/chem.201002094.
[14] L.F. Catañeda, F.F. Rivera, T. Pérez, J.L. Nava, Mathematical modeling and simulation of the reaction environment in electrochemical reactors, Curr. Opin. Electrochem. 16 (2019) 75–82, doi:10.1016/j.coelec.2019.04.025. Electrochemical Materials and Engineering. Sensors and Biosensors
[15] X. He, N. Li, Lattice boltzmann simulation of electrochemical systems, Comput Phys Commun 129 (1) (2000) 158–166, doi:10.1016/S0010-4655(00)00103-X.

[16] S. Gong, P. Cheng, Lattice boltzmann simulation of periodic bubble nucleation, growth and departure from a heated surface in pool boiling, Int J Heat Mass Transf 64 (2013) 122–132, doi:10.1016/j.ijheatmasstransfer.2013.03.058.

[17] M. Sommerfeld, Numerical Methods for Dispersed Multiphase Flows, Springer International Publishing, Cham, 2017, pp. 327–396.

[18] R. Hreiz, L. Abdelouahed, D. Fünfschilling, F. Lapicque, Electrogenerated bubbles induced convection in narrow vertical cells: a review, Chem. Eng. Res. Des. 100 (2015) 268–281, doi:10.1016/j.cherd.2015.05.035.

[19] P. Mandin, A.A. Aissa, H. Roustan, J. Hamburger, G. Picard, Two-phase electrolysis process: from the bubble to the electrochemical cell properties, Chem. Eng. Process. 47 (11) (2008) 1926–1932, doi:10.1016/j.cep.2007.10.018.

[20] P. Mandin, J. Hamburger, S. Bessou, G. Picard, Modelling and calculation of the current density distribution evolution at vertical gas-evolving electrodes, Electrochim. Acta 51 (6) (2005) 1140–1156, doi:10.1016/j.electacta.2005.06.007.

[21] S.S. Deshpande, L. Anumolu, M.F. Trujillo, Evaluating the performance of the two-phase flow solver interFoam, Computational Science & Discovery 5 (1) (2012) 014016, doi:10.1088/1749-4699/5/1/014016.

[22] Y. Renardy, M. Renardy, Prost: a parabolic reconstruction of surface tension for the volume-of-fluid method, J Comput Phys 183 (2) (2002) 400–421, doi:10.1006/jcph.2002.7190.

[23] T. Marić, D.B. Kothe, D. Bothe, Unstructured un-split geometrical volume-of-fluid methods a review, J Comput Phys 420 (2020) 109695, doi:10.1016/j.jcp.2020.109695.

[24] S. Popinet, Numerical models of surface tension, Annu Rev Fluid Mech 50 (1) (2018) 49–75, doi:10.1146/annurev-fluid-122316-045034.

[25] K.J. Vachaparambil, K.E. Einarsrud, Comparison of surface tension models for the volume of fluid method, Processes 7 (8) (2019) 542, doi:10.3390/pr7080542.

[26] K.J. Vachaparambil, K.E. Einarsrud, On sharp surface force model: effect of sharpening coefficient, Experimental and Computational Multiphase Flow 3 (2021) 226232, doi:10.1007/s42757-020-0063-5.

[27] K.J. Vachaparambil, K.E. Einarsrud, Numerical simulation of bubble growth in a supersaturated solution, Appl Math Model 81 (2020) 690–710, doi:10.1016/j.apm.2020.01.017.

[28] D. Deising, H. Marschall, D. Bothe, A unified single-field model framework for volume-of-fluid simulations of interfacial species transfer applied to bubbly flows, Chem Eng Sci 139 (2016) 173–195, doi:10.1016/j.ces.2015.06.021. http://www.sciencedirect.com/science/article/pii/S0009250915004297

[29] J. Maes, C. Soulaine, A new compressive scheme to simulate species transfer across fluid interfaces using the volume-of-fluid method, Chem Eng Sci 190 (2018) 405–418, doi:10.1016/j.ces.2018.06.026.

[30] T. Yamamoto, Y. Okano, S. Dost, Validation of the s-CLSVOF method with the density-scaled balanced continuum surface force model in multiphase systems coupled with thermocapillary flows, Int J Numer Methods Fluids 83 (3) (2017) 223–244, doi:10.1002/fld.4267.

[31] J. Klostermann, K. Schaake, R. Schwarze, Numerical simulation of a single rising bubble by VOF with surface compression, Int J Numer Methods Fluids 71 (8) (2013) 960–982, doi:10.1002/fld.3692.

[32] D. Bothe, S. Fleckenstein, A volume-of-fluid-based method for mass transfer processes at fluid particles, Chem Eng Sci 101 (2013) 283–302, doi:10.1016/j.ces.2013.05.029.

[33] M. Falcone, H. Marschall, Explicit radial-basis-function-based finite-difference method for interfacial mass-transfer problems, Chemical Engineering & Technology 40 (8) (2017) 1385–1390, doi:10.1002/ceat.201600536.

[34] K.J. Vachaparambil, K.E. Einarsrud, Modeling interfacial mass transfer driven bubble growth in supersaturated solutions, AIP Adv 10 (10) (2020) 105024, doi:10.1063/5.0020210.

[35] J. Maes, C. Soulaine, A unified single-field volume-of-fluid-based formulation for multi-component interfacial transfer with local volume changes, J Comput Phys 402 (2020) 109024, doi:10.1016/j.jcp.2019.109024.

[36] H. Liu, L.-m. Pan, J. Wen, Numerical simulation of hydrogen bubble growth at an electrode surface, Can J Chem Eng 94 (1) (2016) 192–199, doi:10.1002/cjce.22378.

[37] C.W. Tobias, Effect of gas evolution on current distribution and ohmic resistance in electrolyzers, J Electrochem Soc 106 (9) (1959) 833, doi:10.1149/1.2427506.

[38] P.J. Sides, Primary potential and current distribution around a bubble on an electrode, J Electrochem Soc 127 (2) (1980) 288, doi:10.1149/1.2129657.

[39] K.E. Einarsrud, S.T. Johansen, Modelling of bubble behaviour in aluminium reduction cells, Progress in Computational Fluid Dynamics, an International Journal 12 (2–3) (2012) 119–130, doi:10.1504/PCFD.2012.047455.

[40] K.E. Einarsrud, I. Eick, W. Bai, Y. Feng, J. Hua, P.J. Witt, Towards a coupled multi-scale, multi-physics simulation framework for aluminium electrolysis, Appl Math Model 44 (2017) 3–24, doi:10.1016/j.apm.2016.11.011.

[41] K.J. Vachaparambil, K.E. Einarsrud, On modelling electrochemical gas evolution using the volume of fluid method, in: J.E. Olsen, J.H. Cloete, S.T. Johansen (Eds.), Proceedings from the 14th International Conference on CFD in Oil & Gas, Metallurgical and Process Industries (CFD2020), SINTEF Academic Press, 2020, pp. 17–27. https://hdl.handle.net/11250/2720838

[42] D. Umehara, S. Hirai, Coupled simulation of bubbles behavior and ion transport and reaction on alkaline water electrolysis, Transactions of the JSME (in Japanese) 84 (865) (2018) 18–00040–18–00040, doi:10.1299/transjsme.18-00040.

[43] M. Sun, B. Li, L. Li, A multi-scale mathematical model of growth and coalescence of bubbles beneath the anode in an aluminum reduction cell, Metallurgical and Materials Transactions B 49 (5) (2018) 2821–2834, doi:10.1007/s11663-018-1311-y.

[44] Z. Zhang, W. Liu, M.L. Free, Phase-field modeling and simulation of gas bubble coalescence and detachment in a gas-liquid two-phase electrochemical system, J Electrochem Soc 167 (1) (2020) 013532, doi:10.1149/2.0322001jes.

[45] A. Taqieddin, R. Nazari, L. Rajic, A. Alshawabkeh, Review—physicochemical hydrodynamics of gas bubbles in two phase electrochemical systems, J Electrochem Soc 164 (13) (2017) E448–E459, doi:10.1149/2.1161713jes.

[46] J. Massing, G. Mutschke, D. Baczyzmalski, S.S. Hossain, X. Yang, K. Eckert, C. Cierpka, Thermocapillary convection during hydrogen evolution at micro-electrodes, Electrochim. Acta 297 (2019) 929–940, doi:10.1016/j.electacta.2018.11.187.

[47] D.M.F. Santos, C.A.C. Sequeira, J.L. Figueiredo, Hydrogen production by alkaline water electrolysis, Quamica Nova 36 (2013) 1176–1193, doi:10.1590/S0100-40422013000800017.

[48] J.A. Leistra, Voltage components at gas evolving electrodes, J Electrochem Soc 134 (10) (1987) 2442, doi:10.1149/1.2100218.

[49] K.J. Vachaparambil, CSECGEFoam, (https://github.com/kurianjv/CSECGEFoam). [Online; accessed 19-December-2020].

[50] P. Cifani, W.R. Michalek, G.J.M. Priems, J.G.M. Kuerten, C.W.M. van der Geld, B.J. Geurts, A comparison between the surface compression method and an interface reconstruction method for the VOF approach, Computers & Fluids 136 (2016) 421–435, doi:10.1016/j.compfluid.2016.06.026.

[51] H. Marschall, K. Hinterberger, C. Schüler, F. Habla, O. Hinrichsen, Numerical simulation of species transfer across fluid interfaces in free-surface flows using openFOAM, Chem Eng Sci 78 (2012) 111–127, doi:10.1016/j.ces.2012.02.034.

[52] M. Wörner, W. Sabisch, G. Grötzbach, D.G. Cacuci, Volume-averaged conservation equations for volume-of-fluid interface tracking, in: Proceedings of the 4th International Conference on Multiphase Flow, 2001. New Orleans, Louisiana, U.S.A

[53] M. Niethammer, G. Brenn, H. Marschall, D. Bothe, An extended volume of fluid method and its application to single bubbles rising in a viscoelastic liquid, J Comput Phys 387 (2019) 326–355, doi:10.1016/j.jcp.2019.02.021.

[54] A.Q. Raeini, M.J. Blunt, B. Bijeljic, Modelling two-phase flow in porous media at the pore scale using the volume-of-fluid method, J Comput Phys 231 (17) (2012) 5653–5668, doi:10.1016/j.jcp.2012.04.011.

[55] S. Hardt, F. Wondra, Evaporation model for interfacial flows based on a continuum-field representation of the source terms, J Comput Phys 227 (11) (2008) 5871–5895, doi:10.1016/j.jcp.2008.02.020.

[56] C. Kunkelmann, Numerical Modeling and Investigation of Boiling Phenomena, Technische Universität, Darmstadt, 2011 Ph.D. thesis. http://tuprints.ulb.tu-darmstadt.de/2731/

[57] M. Bazant, Lecture Notes on Transport in Bulk Electrolytes, 2014, (https://ocw.mit.edu/courses/chemical-engineering/10-626-electrochemical-energy-systems-spring-2014/lecture-notes/) [Online; accessed 18-December-2020].

[58] C. Greenshields, Predictor-Corrector Semi-Implicit MULES, 2014, (https://openfoam.org/release/2-3-0/multiphase/), [Online; accessed 6-July-2020].

[59] D.A. Hoang, V.v. Steijn, L.M. Portela, M.T. Kreutzer, C.R. Kleijn, Benchmark numerical simulations of segmented two-phase flows in microchannels using the volume of fluid method, Computers & Fluids 86 (2013) 28–36, doi:10.1016/j.compfluid.2013.06.024.

[60] R.I. Issa, Solution of the implicitly discretised fluid flow equations by operator-splitting, J Comput Phys 62 (1) (1986) 40–65, doi:10.1016/0021-9991(86)90099-9.

[61] C.J. Greenshields, OpenFOAM User Guide version 7, The OpenFOAM Foundation, 2019. http://foam.sourceforge.net/docs/Guides-a4/OpenFOAMUserGuide-A4.pdf.

[62] C.M. Rhie, W.L. Chow, Numerical study of the turbulent flow past an airfoil with trailing edge separation, AIAA Journal 21 (11) (1983) 1525–1532, doi:10.2514/3.8284.

[63] K. Zeng, D. Zhang, Recent progress in alkaline water electrolysis for hydrogen production and applications, Prog Energy Combust Sci 36 (3) (2010) 307–326, doi:10.1016/j.pecs.2009.11.002.

[64] R. Sander, Compilation of henry's law constants (version 4.0) for water as solvent, Atmos. Chem. Phys. 15 (8) (2015) 4399–4981, doi:10.5194/acp-15-4399-2015.

[65] H. Vogt, On the supersaturation of gas in the concentration boundary layer of gas evolving electrodes, Electrochim. Acta 25 (5) (1980) 527–531, doi:10.1016/0013-4686(80)87052-6.

[66] S. Hysing, S. Turek, D. Kuzmin, N. Parolini, E. Burman, S. Ganesan, L. Tobiska, Quantitative benchmark computations of two-dimensional bubble dynamics, Int J Numer Methods Fluids 60 (11) (2009) 1259–1288, doi:10.1002/fld.1934.

[67] C. Galusinski, P. Vigneaux, On stability condition for bifluid flows with surface tension: application to microfluidics, J Comput Phys 227 (12) (2008) 6140–6164, doi:10.1016/j.jcp.2008.02.023.

[68] S.J. Hashemi, J. Abedi, Advances in modeling of new phase growth, Energy & Fuels 21 (4) (2007) 2147–2155, doi:10.1021/ef060643l.

[69] L.E. Scriven, On the dynamics of phase growth, Chem Eng Sci 10 (1) (1959) 1–13, doi:10.1016/0009-2509(59)80019-1.

[70] X. Yang, F. Karnbach, M. Uhlemann, S. Odenbach, K. Eckert, Dynamics of single hydrogen bubbles at a platinum microelectrode, Langmuir 31 (29) (2015) 8184–8193, doi:10.1021/acs.langmuir.5b01825.

[71] A. Moreno Soto, T. Maddalena, A. Fraters, D. van der Meer, D. Lohse, Coalescence of diffusively growing gas bubbles, J Fluid Mech 846 (2018) 143–165, doi:10.1017/jfm.2018.277.

[72] J.U. Brackbill, D.B. Kothe, C. Zemach, A continuum method for modeling surface tension, J Comput Phys 100 (2) (1992) 335–354, doi:10.1016/0021-9991(92)90240-Y.

[73] N. Samkhaniani, M.R. Ansari, Numerical simulation of bubble condensation using CF-VOF, Prog. Nucl. Energy 89 (2016) 120–131, doi:10.1016/j.pnucene.2016.02.004.

[74] S. Pavuluri, J. Maes, F. Doster, Spontaneous imbibition in a microchannel: analytical solution and assessment of volume of fluid formulations, Microfluid Nanofluidics 22 (8) (2018) 90, doi:10.1007/s10404-018-2106-9.

[75] A. Ashish Saha, S.K. Mitra, Effect of dynamic contact angle in a volume of fluid (VOF) model for a microfluidic capillary flow, J Colloid Interface Sci 339 (2) (2009) 461–480, doi:10.1016/j.jcis.2009.07.071.

[76] H. Schlichting, K. Gersten, Boundary–layer equations in plane flow; plate boundary layer, Boundary-Layer Theory, Springer Berlin Heidelberg, Berlin, Heidelberg, 2017. 145–164, 10.1007/978-3-662-52919-5_6